Ocean Sci., 18, 67–88, 2022
https://doi.org/10.5194/os-18-67-2022

Ocean Science Open Access EGU

A framework to evaluate and elucidate the driving mechanisms of coastal sea surface pCO_2 seasonality using an ocean general circulation model (MOM6-COBALT)

Alizée Roobaert[1], Laure Resplandy[2,3], Goulven G. Laruelle[1], Enhui Liao[2], and Pierre Regnier[1]

[1]Department of Geosciences, Environment & Society-BGEOSYS, Université Libre de Bruxelles, Brussels, Belgium
[2]Department of Geosciences, Princeton University, Princeton, NJ, USA
[3]High Meadows Environmental Institute, Princeton University, Princeton, NJ, USA

Correspondence: Alizée Roobaert (alizee.roobaert@ulb.be)

Received: 17 July 2021 – Discussion started: 18 August 2021
Revised: 22 October 2021 – Accepted: 16 November 2021 – Published: 10 January 2022

Abstract. The temporal variability of the sea surface partial pressure of CO_2 (pCO_2) and the underlying processes driving this variability are poorly understood in the coastal ocean. In this study, we tailor an existing method that quantifies the effects of thermal changes, biological activity, ocean circulation and freshwater fluxes to examine seasonal pCO_2 changes in highly variable coastal environments. We first use the Modular Ocean Model version 6 (MOM6) and biogeochemical module Carbon Ocean Biogeochemistry And Lower Trophics version 2 (COBALTv2) at a half-degree resolution to simulate coastal CO_2 dynamics and evaluate them against pCO_2 from the Surface Ocean CO_2 Atlas database (SOCAT) and from the continuous coastal pCO_2 product generated from SOCAT by a two-step neuronal network interpolation method (coastal Self-Organizing Map Feed-Forward neural Network SOM-FFN, Laruelle et al., 2017). The MOM6-COBALT model reproduces the observed spatiotemporal variability not only in pCO_2 but also in sea surface temperature, salinity and nutrients in most coastal environments, except in a few specific regions such as marginal seas. Based on this evaluation, we identify coastal regions of "high" and "medium" agreement between model and coastal SOM-FFN where the drivers of coastal pCO_2 seasonal changes can be examined with reasonable confidence. Second, we apply our decomposition method in three contrasted coastal regions: an eastern (US East Coast) and a western (the Californian Current) boundary current and a polar coastal region (the Norwegian Basin). Results show that differences in pCO_2 seasonality in the three regions are controlled by the balance between ocean circulation and biological and thermal changes. Circulation controls the pCO_2 seasonality in the Californian Current; biological activity controls pCO_2 in the Norwegian Basin; and the interplay between biological processes and thermal and circulation changes is key on the US East Coast. The refined approach presented here allows the attribution of pCO_2 changes with small residual biases in the coastal ocean, allowing for future work on the mechanisms controlling coastal air–sea CO_2 exchanges and how they are likely to be affected by future changes in sea surface temperature, hydrodynamics and biological dynamics.

1 Introduction

The ocean plays an important role in offsetting human-induced carbon dioxide (CO_2) emissions associated with cement production and fossil fuel combustion (Friedlingstein et al., 2019). Globally, the ocean is a net sink that absorbs roughly one-quarter of the anthropogenic CO_2 emitted into the atmosphere (-2.5 ± 0.6 petagram of carbon per year ($Pg\,C\,yr^{-1}$) for the 2009–2018 decade, Friedlingstein et al., 2019). The spatiotemporal variability of this oceanic CO_2 uptake is relatively well constrained in the open ocean thanks to several methods including sea surface CO_2 data-derived interpolations (e.g., Landschützer et al., 2014; Rödenbeck et al., 2014, 2015; Takahashi et al., 2002), models and atmospheric inversions (e.g., Gruber et al., 2009, 2019; Keeling and Manning, 2014; Manning and Keeling, 2006), but

it is less constrained and understood in the coastal ocean. Nonetheless, in recent decades, significant progress has been made with regard to the quantification and analysis of the spatial distribution of the coastal air–sea CO_2 exchange (FCO_2) globally and regionally (e.g., Borges et al., 2005; Cai, 2011; Chen et al., 2013; Laruelle et al., 2010, 2014; Roobaert et al., 2019). The FCO_2 seasonal cycle was also recently analyzed in coastal regions worldwide by Roobaert et al. (2019). This study identified that at the annual timescale the global coastal ocean acts as an atmospheric CO_2 sink ($-0.2 \pm 0.02\,\mathrm{Pg\,C\,yr^{-1}}$), with a more intense CO_2 uptake occurring in boreal summer because of the disproportionate contribution of high-latitude coastal regions in the Northern Hemisphere, which cover 25 % of the total coastal area and are characterized by an intense CO_2 sink in summer. A more in-depth analysis also revealed that the majority of the coastal seasonal FCO_2 variations stems from the air–sea gradient in partial pressure of CO_2 (pCO_2), although changes in wind speed and sea ice cover can be significant regionally.

Several processes influence the seasonal variations of surface ocean pCO_2 and thus the seasonality in FCO_2. These processes include changes in sea surface temperature (SST) tied to air–sea heat fluxes and ocean circulation, changes in sea surface salinity (SSS) associated with evaporation, freshwater fluxes (from land, ice melt, precipitation and evaporation) and ocean circulation, as well as variations in sea surface alkalinity (ALK) and dissolved inorganic carbon (DIC) tied to biological activity, freshwater fluxes and ocean circulation (Sarmiento and Gruber, 2006). In the open ocean, the respective influence of these processes on the pCO_2 variability has been interpreted using changes in SST, SSS, ALK and DIC observed in situ (e.g., Landschützer et al., 2018; Takahashi et al., 1993) or based on global and regional ocean biogeochemical models relying on a mechanistic, quantitative description of the physical, chemical and biological processes controlling the ocean carbon cycle (e.g., Doney et al., 2009). These investigations reveal that changes in SST (i.e., the thermal effect) are the main driver of the seasonal pCO_2 in tropical oceanic regions, while non-thermal components (change associated with DIC, ALK and SSS) dominate at midlatitudes and high latitudes (poleward of 40° N and 40° S, e.g., Landschützer et al., 2018; Takahashi et al., 2002).

In the coastal ocean, the processes controlling the pCO_2 seasonal dynamics were mostly investigated regionally (e.g., Arruda et al., 2015; Frankignoulle and Borges, 2001; Laruelle et al., 2014; Nakaoka et al., 2006; Shadwick et al., 2010, 2011; Signorini et al., 2013; Turi et al., 2014; Yasunaka et al., 2016), and only a few observation-based studies attempted to analyze the coastal pCO_2 seasonal variability into processes at the global scale (Cao et al., 2020; Chen and Hu, 2019; Laruelle et al., 2017). Regional studies using either observations or model results have covered, e.g., the shelves of the entire Atlantic Basin (Laruelle et al., 2014), the US West Coast (California Current, Turi et al., 2014), US East Coast (e.g., Shadwick et al., 2010, 2011; Signorini et al., 2013), the southern and southeastern Brazilian shelves, the Uruguayan and Patagonia shelves, and shelves in the SW Atlantic Ocean (Arruda et al., 2015). In the California Current, the strong upwelling of carbon-rich waters was identified as the main control of the pCO_2 seasonality (Turi et al., 2014). On the Patagonia shelf, the thermal effect and biological pumps were found to be the main drivers of the seasonal pCO_2 variability, with only a small contribution from the ocean circulation (Arruda et al., 2015), while along the US East Coast seasonal thermal changes play the major role (Shadwick et al., 2010, 2011; Laruelle et al., 2015; Signorini et al., 2013). These studies are, however, confined to specific regions and a global picture of the mechanisms driving the coastal pCO_2 dynamics is still missing. In addition, the attribution analysis of specific physical and biological processes is incomplete. Indeed, the attribution relies on a linear decomposition linking variations in sea surface ocean pCO_2 to seasonal changes in DIC, ALK, SST and SSS (e.g., Signorini et al., 2013, Doney et al., 2009; Lovenduski et al., 2007; Takahashi et al., 1993; Turi et al., 2014) or on a series of sequential simulations isolating biological and physical terms and thus ignores how covariations between the different terms dampen or reinforce each other (e.g., Arruda et al., 2015; Turi et al., 2014).

In this study, we develop a new framework to elucidate the seasonal pCO_2 dynamics of the global coastal ocean. This framework relies on the global Modular Ocean Model version 6 (MOM6, Adcroft et al., 2019) from the NOAA Geophysical Fluid Dynamics Laboratory coupled to the biogeochemical module Carbon Ocean Biogeochemistry And Lower Trophics version 2 (COBALTv2, Stock et al., 2014, 2020). MOM6-COBALT model outputs provide the relevant variables and processes that are required to perform an explicit decomposition of the inorganic carbon dynamics (Liao et al., 2020) in the entire coastal domain. These outputs are then analyzed using a novel approach to attribute seasonal variations in surface ocean pCO_2 to changes in biological activity, ocean circulation, SST, air–sea CO_2 fluxes and freshwater fluxes (Liao et al., 2020) and which is here enhanced for the coastal ocean. The decomposition method constitutes a significant improvement upon previous studies. First, it accounts for co-variations in biological and physical processes and how their evolution jointly modulates the pCO_2 signal. Second, it improves on the traditional linear approaches developed for the open ocean (Sarmiento and Gruber, 2006; Takahashi et al., 1993) and used since then (e.g. Lovenduski et al., 2007) because, as shown later in this study, the linear decomposition introduces significant biases in coastal waters due to the larger range in DIC, ALK, pH and salinity values encountered in the variable coastal environment (Egleston et al., 2010).

In light of these knowledge gaps, the objective of this paper are twofold.

- First, we evaluate the performance of the MOM6-COBALT model in its ability to reproduce the observed spatiotemporal fields of SSS, SST, sea surface nutrients and pCO_2 in the global coastal domain. In particular, we identify the coastal regions where the model best reproduces the observed ocean pCO_2 variability and can thus be considered most suitable for a detailed analysis of the drivers of the pCO_2 seasonal changes.
- Second, to illustrate the capabilities of our upgraded decomposition framework, we examine the drivers of the pCO_2 seasonality in three contrasted coastal regions: the US East Coast, the US West Coast and the Norwegian Basin.

2 Methodology

2.1 Ocean biogeochemical model description

In this study, we used the ocean model MOM6 and the Sea Ice Simulator version 2 (fourth generation of ocean ice models, OM4) detailed in Adcroft et al. (2019). The version of OM4 adopted here is OM4p5 which has a nominal horizontal resolution of 0.5° (i.e., with a finer latitudinal resolution of 0.26° in the tropical region). In the vertical, it includes 75 hybrid coordinates with a z^* coordinate near the surface (geopotential coordinate allowing free surface undulations) and a modified potential density coordinate below. The vertical spacing increases from 2 m in the upper 20 m (i.e., first 10 layers) to larger isopycnal layers below. Layers in z^* broadly deepen towards high latitudes (see Adcroft et al., 2019, for details on the grid). This ocean ice model is coupled to the biogeochemical module COBALT version 2 (COBALTv2), which includes 33 state variables to resolve global-scale cycles of carbon, nitrogen, phosphate, silicate, iron, calcium carbonate, oxygen and lithogenic materials (Stock et al., 2020). Details about the planktonic food web dynamics in COBALT, and global assessments of large-scale carbon fluxes through the food web, such as net primary production, can be found in Stock et al. (2014, 2020). The ocean model is forced by the 55 km horizontal resolution Japanese atmospheric reanalysis (JRA55-do) version 1.3 at a 3 h frequency between 1959 and 2018 (Tsujino et al., 2018), and the atmospheric CO_2 concentration data (xCO_2) from the Earth System Research Laboratory (Conway et al., 1994; Masarie, 2012). The xCO_2 is converted to pCO_2 using atmospheric and water vapor pressures by the model. SST, SSS, sea surface nutrients (nitrate, phosphate, silicate) and oxygen were initialized from the World Ocean Atlas version 2013 (Garcia et al., 2013a, b; Locarnini et al., 2013; Zweng et al., 2013). Initial DIC and ALK conditions are taken from GLODAPv2 (Olsen et al., 2016). The initial DIC is corrected for the accumulation of anthropogenic carbon to match the level expected in the first year of the simulation (1959) using the data-based estimate of ocean anthropogenic carbon content of Khatiwala et al. (2013). At the end of an 81-year spin-up repeating the year 1959, the model reached a near-equilibrium between atmospheric pCO_2 and surface ocean pCO_2, with a drift in global air–sea CO_2 flux $< 0.004\,\mathrm{Pg\,C\,yr^{-1}}$ over the last 10 years of the spin-up. Further details on the configuration, spin-up and simulation can be found in Liao et al. (2020).

2.2 Observational products and model evaluation

We first evaluate the ability of MOM6-COBALT to reproduce the observed spatial distribution of environmental variables in the coastal domain, namely the SST, SSS and sea surface nutrients (nitrate, phosphate and silicate). The observational SST and SSS fields are from the daily NOAA OI SST V2 (Reynolds et al., 2007) and the daily Hadley center EN4 SSS (Good et al., 2013), respectively. The observed nutrient fields in the sea surface are extracted from the World Ocean Atlas version 2018 (Garcia et al., 2019). We also compare the simulated coastal pCO_2 directly to uninterpolated observations extracted from the Surface Ocean CO_2 Atlas database (SOCAT) using monthly observations from SOCAT version 6 gridded at the spatial resolution of 0.25° (SOCATv6, Bakker et al., 2016). For the evaluation period used in this study (1998–2015), this database contains 9.8 million pCO_2 observations within the coastal domain. All data from SOCATv6 are converted from fugacity of CO_2 in water to pCO_2 using the formulation of Takahashi et al. (2012). We finally compare the pCO_2 simulated by the MOM6-COBALT model to the 0.25° continuous monthly pCO_2 fields generated from the SOCAT observations by the two-step neuronal network (Self-Organizing Map Feed-Forward neural Network, SOM-FFN) in coastal regions (Laruelle et al., 2017). The SOM-FFN data product of Laruelle et al. (2017) is thus not "raw" and implies a significant amount of statistical modeling. It is also derived from an earlier version of SOCAT (SOCATv4, Laruelle et al., 2017) than the one used in this study. In what follows, the pCO_2 products generated by the model, the statistical interpolation of observations, and the un-interpolated observations will be referred to as MOM6-COBALT, coastal SOM-FFN and SOCATv6, respectively. All observational and simulated fields are converted from their original spatiotemporal resolution to monthly 0.25° gridded climatologies for the 1998–2015 period to match the one used by the coastal SOM-FFN. Cells that are covered by more than 95 % sea ice are removed from the comparison since we assume no transfer of our master variable (pCO_2) through sea ice. In our analysis, we apply the broad definition of the coastal zone by Laruelle et al. (2017), using a global mask that excludes estuaries and inland water bodies, while its outer limit is set 300 km away from the shoreline. This definition leads to a total surface area of 77 million km^2, which is split into 45 coastal regions using the MARgins and CATchment Segmentation (MARCATS, Laruelle et al., 2013). These 45 regions are grouped

into seven broad classes with similar hydrological and climatic settings (Liu et al., 2010): (1) an Eastern Boundary Current and (2) Western Boundary Current (EBC and WBC, respectively), (3) tropical margins, (4) subpolar and (5) polar margins, (6) marginal seas, and (7) Indian margins.

The model evaluation of all gridded environmental variables including pCO_2 is performed for the annual mean and the seasonal cycle both globally and within each of the 45 MARCATS regions. For the seasonal analysis a climatological monthly anomaly is calculated, for each variable, as the difference between the variable x for a given month and its climatological annual mean. The evaluation of the seasonal amplitude is then performed using the bias between observed and simulated root mean square (rms) of their monthly anomalies. A positive bias represents a larger simulated seasonal amplitude than derived from the observations. The temporal shift between the observed and simulated seasonal cycles is also assessed from the Pearson correlation coefficient (no units) of the regression between monthly times series simulated by MOM6-COBALT and those extracted from the observations. These comparisons not only serve to assess the overall model performance in reproducing observations but also help to identify potential discrepancies between observed and simulated environmental fields (e.g., SST, SSS) that are used by the two-step neuronal network coastal SOM-FFN to generate the continuous pCO_2 climatology. We use two metrics to evaluate SOCATv6 spatial and temporal coverage. First, we evaluate the spatial coverage at the MARCATS region scale by computing the percent surface area sampled by SOCATv6 data for each MARCATS region. A 50 % spatial coverage means that SOCATv6 data are available in 50 % of the $0.25° \times 0.25°$ cells included in this specific MARCATS region (this metric is used in Fig. 1a). Second, we evaluate the ability of SOCATv6 to capture the seasonality at the grid cell scale by computing the number of months where there is at least one SOCATv6 pCO_2 measurement for each $0.25° \times 0.25°$ grid cell. An 8-month temporal coverage means that 8 out of the 12 months are sampled at least once in this grid cell (this metric is used in Fig. 6a).

Finally, from this global and regional spatiotemporal evaluation, we label the agreement between the model and coastal SOM-FFN ("high", "medium" and "low") for each MARCATS region and identify regions for which our results are the most robust for further in-depth analysis of the processes driving the coastal pCO_2 dynamics. The labels of agreement are based on three criteria. First, we assess whether the simulated annual mean pCO_2 is within 20 µatm of the one extracted from the coastal SOM-FFN. This threshold of 20 µatm roughly corresponds to the globally averaged pCO_2 gradient between the atmosphere and the coastal sea surface (Laruelle et al., 2018). The second and third criteria evaluate the magnitude and phasing of the simulated pCO_2 seasonal cycle against the coastal SOM-FFN using an absolute bias in the seasonal magnitude <20 µatm and a Pearson coefficient > 0.5 as a threshold. The agreement is considered "high" when the three criteria are fulfilled, "medium" when criteria 2 and 3 are satisfied, and "low" when only one (or no) criterion is met for the seasonality.

2.3 Processes controlling seasonal pCO_2 variability: a method tailored for coastal regions

The pCO_2 in surface sea water can be computed from DIC and ALK following Eq. (1) (Sarmiento and Gruber, 2006; Wolf-Gladrow et al., 2007):

$$pCO_2 = \frac{K_2'}{K_0' K_1'} \frac{(2\mathrm{DIC} - \mathrm{ALK})^2}{\mathrm{ALK} - \mathrm{DIC}}, \quad (1)$$

where K_0' is the aqueous-phase solubility constant of CO_2 in water and K_1' and K_2' represent the apparent equilibrium dissociation constants of the carbonate system. Several physical and biogeochemical processes can thus affect pCO_2 via changes in DIC, ALK and/or via the $\frac{K_2'}{K_0' K_1'}$ term, which depends on SST and SSS. To quantify the processes controlling the pCO_2 variability at the seasonal timescale of interest to this study, we adopt the method of Liao et al. (2020). The method starts from the traditional approach that links variations in sea surface ocean pCO_2 to changes in DIC, ALK, SST and SSS using the following linear decomposition (Doney et al., 2009; Lovenduski et al., 2007; Takahashi et al., 1993; Turi et al., 2014):

$$\Delta pCO_2 \approx \frac{\partial pCO_2}{\partial \mathrm{DIC}} \Delta\mathrm{DIC} + \frac{\partial pCO_2}{\partial \mathrm{ALK}} \Delta\mathrm{ALK} + \frac{\partial pCO_2}{\partial \mathrm{SST}} \Delta\mathrm{SST} + \frac{\partial pCO_2}{\partial \mathrm{SSS}} \Delta\mathrm{SSS}, \quad (2)$$

where Δx terms represent the seasonal anomaly of x (i.e., the departure from the annual mean) and $\frac{\partial pCO_2}{\partial \mathrm{DIC}}$, $\frac{\partial pCO_2}{\partial \mathrm{ALK}}$, $\frac{\partial pCO_2}{\partial \mathrm{SST}}$ and $\frac{\partial pCO_2}{\partial \mathrm{SSS}}$ are coefficients that describe the sensitivity of pCO_2 to changes in DIC, ALK, SST and SSS, respectively. The coefficients for DIC, SST and SSS are always positive as pCO_2 increases with increases in DIC, SST or SSS, while the coefficient for ALK is always negative as pCO_2 systematically decreases with increasing ALK. These coefficients are generally estimated using the approach of Sarmiento and Gruber (2006) (see Eqs. S1–S4 in the Supplement), which has been widely used in the open ocean (Liao et al., 2020; Sarmiento and Gruber, 2006; Takahashi et al., 1993). In this study, we refine the estimation of the coefficients so they can be used for the wide range of DIC / ALK ratios that can be encountered in the coastal waters. This includes conditions when the DIC / ALK ratio is close to 1, such as in regions with significant freshwater discharge like those found near estuarine mouths or on polar shelves subject to sea ice melting when pH is around 7.5 (Egleston et al., 2010). In these cases, the traditional approximation method using mean DIC, ALK, SSS and SST fields breaks down (see Eqs. S1–S2 and Fig. S1 in the Supplement). To circumvent this important limitation, we computed the coefficients of the pCO_2 dependency using a regression approach

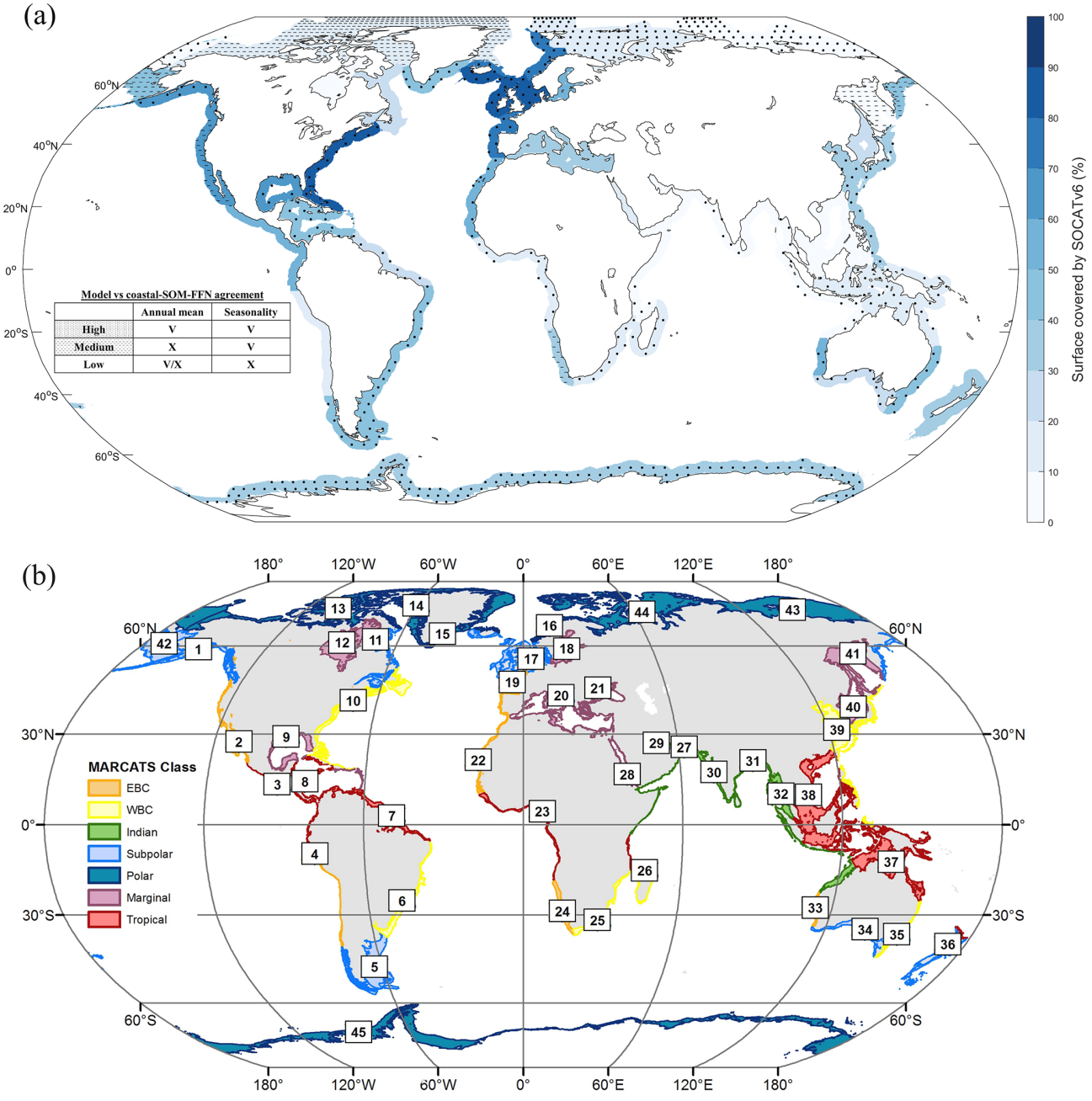

Figure 1. **(a)** SOCATv6 spatial coverage (color) and agreement between model and coastal SOM-FFN product (symbols) in coastal MARCATS (Margins and CATchment Segmentation) regions. The blue intensity indicates the fraction of the MARCATS region's surface area covered by SOCATv6 observations (from light to dark blue). Dots indicate where the model fulfills three evaluation criteria ("high" agreement regions) of the spatiotemporal pCO_2 distribution (i.e., annual mean mismatch <20 µatm between MOM6-COBALT and coastal SOM-FFN, Pearson correlation coefficient > 0.5, and seasonal amplitude mismatch <20 µatm). Dashes indicate where the model only fulfills two criteria (seasonal amplitude and phase, "medium" agreement). Other regions ("low" agreement with no symbol) do not fulfill the two criteria associated with seasonality. Details of the model to coastal SOM-FFN agreement are given in Table 1. **(b)** Discretization of the coastal seas into 45 MARCATS regions (Laruelle et al., 2013) grouped into the following seven classes: Eastern Boundary Current (EBC, MARCATS 2, 4, 19, 22, 24 and 33) and Western Boundary Current (WBC, MARCATS 6, 10, 25, 35 and 39), polar (MARCATS 13, 14, 15, 16, 43, 44, and 45) and subpolar margins (MARCATS 1, 5, 11, 17, 34, 36 and 42), tropical margins (MARCATS 3, 7, 8, 23, 26, 37 and 38), Indian margins (MARCATS 27, 30, 31 and 32), and marginal seas (MARCATS 9, 12, 18, 20, 21, 28, 29, 40 and 41).

Table 1. Model vs. coastal SOM-FFN agreement level. For each MARCATS region, the agreement ("high", "medium" and "low") is attributed by the pCO_2 spatiotemporal analysis. Regions where the model fulfills criteria on the annual mean and seasonality are labeled as high-agreement regions (i.e., annual mean mismatch <20 µatm between MOM6-COBALT and coastal SOM-FFN, Pearson correlation coefficient >0.5, and seasonal amplitude mismatch <20 µatm, dots in Fig. 1a). High*-agreement regions can present a bias >20 µatm on the comparison with SOCATv6 (see Table S1 in the Supplement). Medium-agreement regions represent MARCATS regions where the model only fulfills seasonal criteria (seasonal amplitude and phase, dashed in Fig. 1a). Other regions (low agreement) do not fulfill the two criteria associated with the seasonality (no symbol in Fig. 1a). Regions with high agreement are considered the most robust for an in-depth analysis of the processes driving the coastal pCO_2 dynamics and are highlighted in bold.

			Annual mean pCO_2 (µatm)		Seasonal pCO_2			
					Amplitude (µatm)			
MARCATS number (Mx)	MARCATS name	MARCATS category	Coastal SOM-FFN rms	Model bias	Coastal SOM-FFN	Model bias	Phasing (Pearson coefficient)	Model vs. coastal SOM-FFN agreement
2	Californian Current	EBC	360.0	34.5	8.3	16.2	1.0	Medium
4	Peruvian Upwelling Current	EBC	377.6	106.4	4.1	6.6	−0.4	Low
19	**Iberian upwelling**	**EBC**	**354.8**	**9.3**	**7.5**	**15.6**	**0.8**	**High**
22	**Moroccan upwelling**	**EBC**	**379.4**	**10.2**	**7.4**	**8.7**	**0.9**	**High**
24	SW Africa	EBC	349.1	79.3	7.2	4.2	0.9	Medium
33	**Leeuwin Current**	**EBC**	**349.4**	**4.2**	**5.6**	**12.7**	**0.9**	**High**
27	W Arabian Sea	Indian margins	383.5	11.6	8.7	3.6	0.3	Low
30	**E Arabian Sea**	**Indian margins**	**388.4**	**−8.3**	**4.8**	**6.2**	**0.7**	**High**
31	Bay of Bengal	Indian margins	377.3	−24.1	7.4	13.5	−0.2	Low
32	**Tropical E Indian Ocean**	**Indian margins**	**373.3**	**0.3**	**2.3**	**5.4**	**0.9**	**High**
9	**Gulf of Mexico**	**Marginal sea**	**384.3**	**−9.1**	**13.9**	**12.9**	**1.0**	**High**
12	Hudson Bay	Marginal sea	326.4	5.7	65.3	−46.4	0.4	Low
18	Baltic Sea	Marginal sea	336.2	21.4	79.4	−44.4	0.9	Low
20	Mediterranean Sea	Marginal sea	388.1	−11.9	25.1	20.6	1.0	Low
21	Black Sea	Marginal sea	325.0	25.2	141.9	−116.9	−0.5	Low
28	Red Sea	Marginal sea	412.2	−16.5	25.0	−0.4	−0.9	Low
29	Persian Gulf	Marginal sea	411.2	−7.6	31.3	30.7	−0.9	Low
40	Sea of Japan	Marginal sea	330.3	−9.3	21.1	28.0	0.9	Low
41	Sea of Okhotsk	Marginal sea	321.2	29.2	28.6	−6.5	0.7	Medium
13	Canadian Archipelago	Polar	325.4	−53.1	43.4	−18.0	0.9	Medium
14	N Greenland	Polar	306.0	−24.3	21.7	−9.0	0.8	Medium
15	**S Greenland**	**Polar**	**325.2**	**1.3**	**24.5**	**−8.5**	**1.0**	**High**
16	**Norwegian Basin**	**Polar**	**328.1**	**−0.7**	**19.9**	**−6.1**	**0.9**	**High**
43	**Siberian shelves**	**Polar**	**338.2**	**−19.7**	**57.4**	**−15.7**	**0.9**	**High***
44	**Barents and Kara seas**	**Polar**	**311.6**	**−3.3**	**24.9**	**−7.4**	**0.7**	**High**
45	**Antarctic shelves**	**Polar**	**373.7**	**−17.6**	**22.6**	**13.3**	**1.0**	**High***
1	**NE Pacific**	**Subpolar**	**342.5**	**16.8**	**15.8**	**−4.5**	**0.8**	**High***
5	**South America**	**Subpolar**	**351.1**	**14.0**	**12.1**	**−6.4**	**0.8**	**High**
11	Sea of Labrador	Subpolar	326.3	5.5	17.0	0.8	0.2	Low
17	**NE Atlantic**	**Subpolar**	**354.4**	**−4.5**	**14.9**	**−8.2**	**0.6**	**High**
34	**S Australia**	**Subpolar**	**352.7**	**13.5**	**3.7**	**12.8**	**0.9**	**High**
36	New Zealand	Subpolar	352.4	6.1	2.6	6.2	−0.5	Low
42	NW Pacific	Subpolar	337.7	25.2	36.5	−19.2	1.0	Medium
3	Tropical E Pacific	Tropical	382.2	17.2	6.9	3.1	0.3	Low
7	**Tropical W Atlantic**	**Tropical**	**380.3**	**−19.8**	**2.8**	**9.6**	**1.0**	**High**
8	**Caribbean Sea**	**Tropical**	**387.6**	**−1.7**	**6.6**	**2.2**	**1.0**	**High**
23	**Tropical E Atlantic**	**Tropical**	**374.6**	**15.9**	**2.9**	**1.5**	**0.6**	**High***
26	**Tropical W Indian Ocean**	**Tropical**	**384.8**	**4.8**	**7.1**	**5.6**	**0.9**	**High***
37	**N Australia**	**Tropical**	**378.5**	**−4.0**	**4.3**	**5.2**	**1.0**	**High**
38	SE Asia	Tropical	373.5	0.6	2.6	8.9	0.2	Low
6	**Brazilian Current**	**WBC**	**374.8**	**7.0**	**6.7**	**7.5**	**0.9**	**High**
10	**US East Coast**	**WBC**	**368.1**	**−9.6**	**12.0**	**12.4**	**0.9**	**High**
25	**Agulhas Current**	**WBC**	**367.1**	**5.7**	**7.1**	**8.1**	**1.0**	**High**
35	**E Australian Current**	**WBC**	**343.9**	**2.9**	**3.3**	**7.4**	**1.0**	**High**
39	**East China Sea and Kuroshio**	**WBC**	**359.6**	**−4.1**	**10.3**	**13.2**	**0.9**	**High**

based on the CO2SYS program (Lewis and Wallace, 1998). At each point in space, pCO_2 was computed using the 1998–2015 average of DIC, ALK, SSS and SST with CO2SYS (method 14 in the CO2SYS MATLAB program, Millero, 2010). The $\frac{\partial pCO_2}{\partial DIC}$ coefficient was then computed as the slope of the linear regression between pCO_2 and DIC obtained by allowing DIC to vary around the local mean DIC value while keeping other tracers (ALK, SST, SSS) constant. The DIC range used to compute the slope was set to the ± 2 SD of the 1998–2015 monthly values at that location with an upper bound at $\pm 60\,\mu mol\,kg^{-1}$ (see the Supplement for further details). The same approach was repeated to compute the coefficients for the pCO_2 dependence on ALK, SST and SSS, respectively. Our methodology leads to coefficients that are constant in time but are space dependent. In Fig. S1, we compare the coastal pCO_2 reconstructed from the traditional decomposition (using the space-varying coefficients reported by Sarmiento and Gruber, 2006) with those computed here using the CO2SYS regression. For the global coastal ocean, we find a large bias (global mean root-mean-square error (RMSE) of fitting pCO_2 anomaly in Eq. (2) $= 14.6\,\mu atm$), which is especially pronounced at high latitudes. In contrast, the decomposition method based on our methodology drastically reduce the biases (global mean RMSE $= 2.8\,\mu atm$) in coastal regions and allows a more robust reconstruction of the pCO_2 variability.

We further evaluated how using coefficients that vary in both time and space could reduce the residual biases between our pCO_2 decomposition (using space-dependent coefficients that are constant in time) and the pCO_2 simulated in the model that are found in regions with large freshwater discharge, such as the mouth of the Amazon River or Arctic coastal waters. We compare the pCO_2 seasonality simulated by the model to the pCO_2 reconstructed by the following three methods: space-varying coefficients from Sarmiento and Gruber (2006), regression-based space-varying coefficients, and regression-based space- and time-varying coefficients, all of which used a point in the Amazon River plume (1° N, 310.25° E, Fig. S1d and e). At this location, the use of the regression-based coefficients greatly improves the recovery of the simulated pCO_2 compared to using the traditional coefficients of Sarmiento and Gruber (2006), reducing the RMSE from 83 to 24 µatm, corresponding to a bias reduction of 71 %. The use of both space- and time-dependent regression-based coefficients further reduces this bias, bringing down the RMSE from 24 to 18 µatm corresponding to an additional 7 % reduction of the initial bias (83 µatm). Based on these results, we chose to use space dependent only coefficients, which is a simpler approach to implement here and in future studies.

Here we assume that the coefficients are constant in time, and the temporal change in pCO_2 ($\partial_t pCO_2$ in µatm per month) can therefore be expressed as a simple function of the temporal changes in DIC (∂_tDIC), ALK (∂_tALK), SST (∂_tSST) and SSS (∂_tSSS):

$$\partial_t pCO_2 \approx \frac{\partial pCO_2}{\partial DIC}\partial_t DIC + \frac{\partial pCO_2}{\partial ALK}\partial_t ALK + \frac{\partial pCO_2}{\partial SST}\partial_t SST + \frac{\partial pCO_2}{\partial SSS}\partial_t SSS. \quad (3)$$

Temporal changes in DIC, ALK, SST and SSS (∂_fDIC, ∂_tALK, ∂_tSST and ∂_tSSS) are controlled by surface heat flux, ocean transport, freshwater fluxes, biological processes and the air–sea CO_2 flux. Using the model results, we further expand the decomposition to quantify the contribution of these physical and biological processes (see Liao et al, 2020, for details about the derivation):

$$\underbrace{\partial_t pCO_2}_{pCO_2\text{change}} \approx \underbrace{\left(\frac{\partial pCO_2}{\partial DIC}\partial_t DIC_h + \frac{\partial pCO_2}{\partial ALK}\partial_t ALK_h + \frac{\partial pCO_2}{\partial_{SSS}}\partial_t SSS_h + \frac{\partial pCO_2}{\partial DIC}\partial_t DIC_v + \frac{\partial pCO_2}{\partial ALK}\partial_t ALK_v + \frac{\partial pCO_2}{\partial SSS}\partial_t SSS_v\right)}_{\text{circ}} + \underbrace{\left(\frac{\partial pCO_2}{\partial DIC}\partial_t DIC_{fw} + \frac{\partial pCO_2}{\partial ALK}\partial_t ALK_{fw} + \frac{\partial pCO_2}{\partial SSS}\partial_t SSS_{fw}\right)}_{\text{fw}} + \underbrace{\left(\frac{\partial pCO_2}{\partial DIC}\partial_t DIC_{bio} + \frac{\partial pCO_2}{\partial ALK}\partial_t ALK_{bio}\right)}_{\text{bio}} + \underbrace{\left(\frac{\partial pCO_2}{\partial SST}\left(\partial_t SST_h + \partial_t SST_v + \partial_t SST_q\right)\right)}_{\text{thermal}} + \underbrace{\left(\frac{\partial pCO_2}{\partial DIC}\partial_t DIC_{CO_2\,flux}\right)}_{CO_2\text{flux}}, \quad (4)$$

where the temporal changes in pCO_2 (time tendency called pCO_2 change) are on the left-hand side (LHS) of the equation and the five terms that control this change in pCO_2 are on the right-hand side (RHS) of the equation. Subscripted h and v denote the contribution from horizontal (advection and diffusivity in the meridional and zonal directions) and vertical (vertical advection and diffusivity) transports on SST, SSS, DIC, and ALK; "bio" denotes the DIC and ALK changes induced by biological processes (photosynthesis, respiration, calcium carbonate dissolution and precipitation, denitrification, and nitrification); q denotes the effect of surface heat flux on SST; "fw" denotes the effect of freshwater fluxes (i.e., precipitation, evaporation, river runoff, and sea ice formation and melting) on SSS, DIC, and ALK; and the term CO_2 flux denotes the DIC change induced by air–sea CO_2 exchange.

Here we examine changes in pCO_2 attributed to three oceanic processes that modify the concentration in dissolved species (i.e., DIC, ALK and SSS), namely their transport by oceanic circulation ("circ", which includes horizontal and

vertical transport), the effect of dilution and concentration due to freshwater fluxes (fw), and the effect of biological activity (bio), and these processes isolate the thermal influence tied to SST changes induced by both oceanic transport and air–sea exchange of heat. Finally, the air–sea CO_2 exchange (CO_2 flux) pushes the surface pCO_2 concentration towards its equilibrium with the atmosphere and systematically acts to offset the pCO_2 changes associated with the sum of the internal oceanic processes (circ, bio, fw and thermal). In this study, we apply Eq. (4) using averages between the sea surface and the mixed-layer depth (MLD), defined here as the depth where the water density is 0.01 kg m^{-3} denser than the water at the surface (minimum MLD is 5 m). Positive contributions on the RHS would yield an increase in pCO_2 (positive pCO_2 response on the LHS). Positive values of the CO_2 flux correspond to an ocean CO_2 uptake. This method to decompose the pCO_2 seasonality into controlling processes in the coastal domain is illustrated in three coastal regions: the US East Coast, the US West Coast and the Norwegian Basin.

3 Results and discussion

3.1 Annual mean state and seasonal cycle model evaluation and identification of coastal regions

Figure 1a identifies the coastal regions where the performance of MOM6-COBALT is satisfactory for both the annual mean and the seasonal cycle of pCO_2. The analysis, performed at the MARCATS scale (see Fig. 1b for nomenclature), distinguishes regions of low, medium and high agreement between the model and coastal SOM-FFN, the latter being areas for which our confidence in the identification of the dominant biophysical drivers of the coastal pCO_2 dynamics is highest. This figure will be analyzed in detail in Sect. 3.1.3, but before we do so we first perform a data–model evaluation according to the following procedure. We first evaluate the model by comparing simulated fields of SSS, SST and sea surface nutrients to global and regional observations (Sect. 3.1.1, Figs. 2 and 3). Second, the ability of the model to capture the coastal pCO_2 annual mean and seasonality is assessed against the SOCATv6 data and the continuous monthly observation-based pCO_2 product (coastal SOM-FFN, Laruelle et al., 2017; see Sect. 3.1.2 and Figs. 3–6).

3.1.1 Model evaluation for coastal waters environmental variables

MOM6-COBALT captures the main spatial patterns of key environmental parameters (SST, SSS and sea surface nutrients) fairly well in the coastal domain (Fig. 2). The global SST field simulated by the model reproduces the strong large-scale tropical to polar SST gradients, with a global median bias of -0.2 °C (Fig. 2a–c), and biases at the scale of MARCATS regions ranging from 0 °C in the NE Atlantic (M17) to 1.3 °C on the US East Coast (M10, Fig. 3a and Table S1). With a global median bias value of 0.2, the model also correctly reproduces the observed SSS patterns that are mainly regulated by evaporation and freshwater inputs from precipitation, riverine runoff and ice melt, with lower SSS values in polar regions and along the coasts of Southeast Asia and higher SSS values along the coasts of evaporation basins such as in the Arabian Sea or the Mediterranean Sea (Fig. 2d–f). The SSS analysis at the MARCATS scale reveals absolute SSS biases that are generally less than or close to 1, except for five MARCATS regions where absolute biases exceed 2. These MARCATS regions are mainly located in marginal seas (the Baltic Sea, M18; the Black Sea, M21; and the Persian Gulf, M29) but also include one polar region (the Canadian Archipelago, M13) and one tropical region (Tropical West Atlantic, M7; see Fig. 3b and Table S1). Similar to SSS, largest the model–data discrepancies for nutrients are mostly found in marginal seas (Fig. 3c–e and Table S1). For instance, the largest PO_4 and SiO_4 biases are encountered in the Black Sea (M21, absolute biases of 3 and 75 µmol kg^{-1}, respectively). The Peruvian Upwelling Current (M4), the Bay of Bengal (M31) and the NE Pacific (M1) also present large biases in NO_3 and PO_4 (e.g., NO_3 bias of 8 µmol kg^{-1} for M4). However, the global median nutrients biases are much smaller, reaching 0.3, -0.2 and -0.4 µmol kg^{-1} for nitrate (NO_3, Fig. 2i), phosphate (PO_4, Fig. 2l) and silicate (SiO_4, Fig. 2o), respectively.

The model–data seasonal evaluation reveals that MOM6-COBALT reproduces the global SST and SSS amplitudes remarkably well (median absolute bias of 0.1 °C and 0.0, respectively; see Table S2 in the Supplement). Some exceptions can nevertheless be diagnosed, such as in the marginal Black Sea (M21), where the bias in SST seasonal amplitude reaches -1.3 °C, and in three MARCATS regions (Bay of Bengal, M31; tropical West Atlantic, M7; and Siberian shelves, M43) where the SSS seasonal biases are larger than 0.4. The model–data comparison also reveals that the phasing of the SST and SSS seasonal cycles are in very good agreement (Pearson correlation close to 1) for all 45 MARCATS regions, with the exception of four for which significant deviations in SSS are found, i.e., two marginal seas (Hudson Bay, M12, and the Red Sea, M28) and along the Californian Current (M2) and Brazilian Current (M6). The nutrients analysis shows absolute global median biases in seasonal amplitude of 0.1, 0.0 and 0.7 µmol kg^{-1} for NO_3, PO_4 and SiO_4, respectively. Seven MARCATS regions present absolute biases larger than 1.5 µmol kg^{-1} that are mainly located in marginal seas (Baltic Sea, M18; Sea of Japan M40; and Sea of Okhotsk, M41) but also in polar (Siberian, M43, and Antarctic, M45, shelves) and subpolar (NE Pacific, M1) regions and in the Bay of Bengal (M31). The model–data comparison sometimes shows significant phase shifts in their seasonal signal (Pearson coefficient < 0.5), such as for MARCATS regions located in Indian and tropical margins, marginal seas, and EBCs.

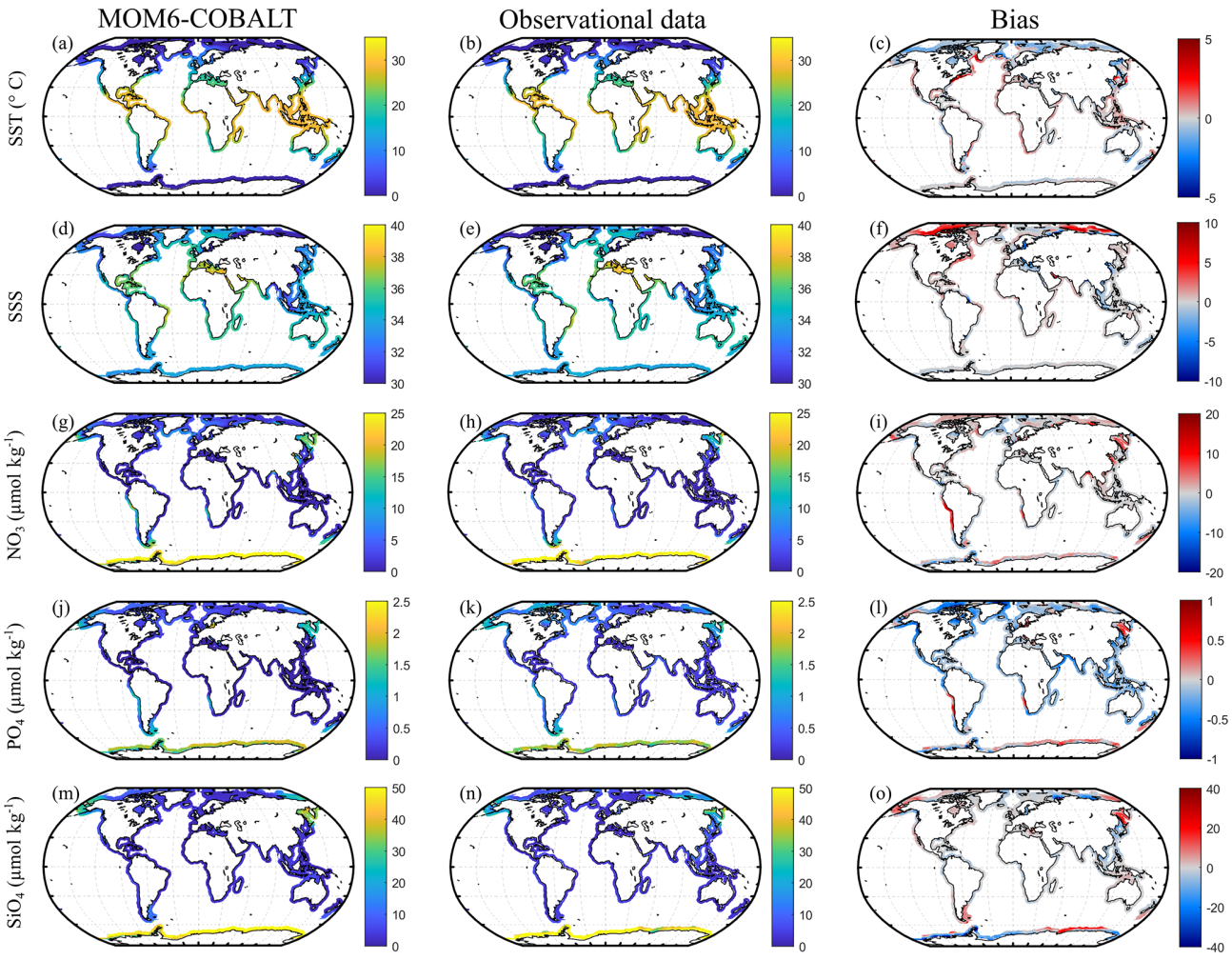

Figure 2. Observed (center) and modeled (left) spatial distributions of the annual mean state of SST (°C), SSS (no unit), nitrate (NO_3, µmol kg^{-1}), phosphate (PO_4, µmol kg^{-1}) and silicate (SiO_4, µmol kg^{-1}) and model annual mean bias (right). Observational SST and SSS fields are from the NOAA OI SST V2 (Reynolds et al., 2007) and the EN4 SSS (Good et al., 2013). Observational nutrients are from the World Ocean Atlas version 2018 (Garcia et al., 2019). The bias is the difference between MOM6-COBALT and observed values (red indicates regions where the simulated variables by MOM6-COBALT exceed observed values).

3.1.2 Model evaluation for coastal pCO_2

The spatial distribution of the annual mean pCO_2 simulated by MOM6-COBALT is in good agreement with the observational pCO_2 values extracted from the SOCATv6 database with generally low pCO_2 values (blue colors) in temperate and high latitudes and high pCO_2 values (yellow and red colors) in tropical and sub-tropical regions (Fig. 4a–c). The model–data pCO_2 evaluation at the regional scale shows that 33 of the 45 MARCATS present absolute biases lower than 20 µatm (Table S1). The regions where the bias exceeds this threshold include two EBCs (the Californian Current, M2, and the Peruvian Upwelling Current, M4), two marginal seas (Sea of Japan, M40, and Sea of Okhotsk, M41), and one polar region (Antarctic shelves, M45), a subpolar region (NW Pacific, M42) and the tropical East Atlantic (M23) shelf. Note that in some MARCATS regions, in particular in marginal seas and Indian seas, there are no SOCATv6 observations to perform the comparison (e.g., the Bay of Bengal, M31; see Fig. 4b and Table S1). Hence, we also evaluate the performance of MOM6-COBALT against the continuous coastal SOM-FFN pCO_2 product, which uses a neural network interpolation method to fill data gaps and resolve the spatiotemporal coastal pCO_2 variability globally.

Our results show that MOM6-COBALT reproduces the main spatial features of the annual mean pCO_2 field captured by the coastal SOM-FFN product, as revealed by the relatively low globally averaged bias of 2.5 µatm (Fig. 4a and d). In both the model and the SOM-FFN product, low coastal pCO_2 values are consistently found in temperate and high-latitude regions in both hemispheres, while high pCO_2 values are largely limited to (sub-)tropical regions. The largest

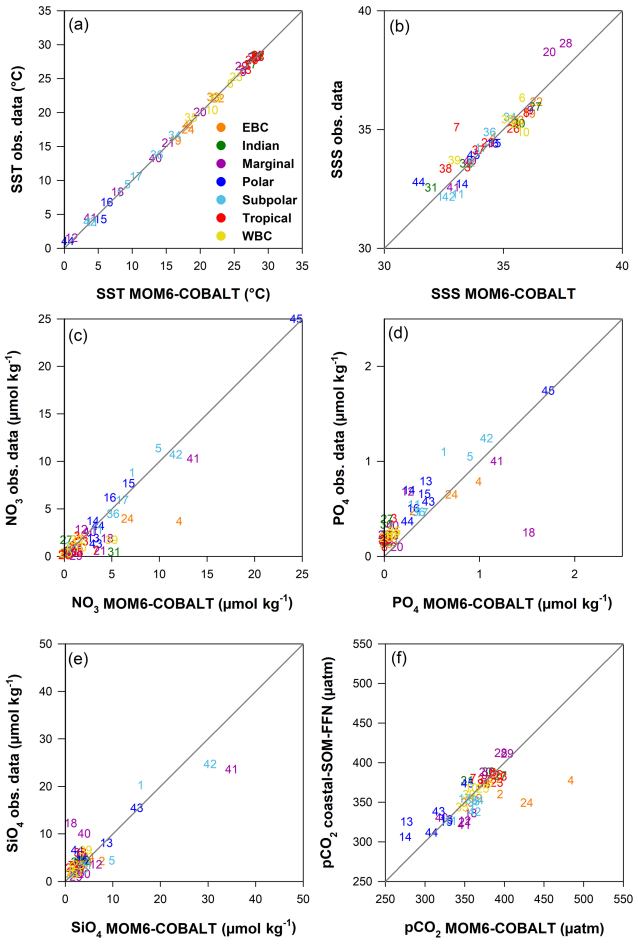

Figure 3. Comparison between observed and simulated annual mean fields in the 45 MARCATS regions: **(a)** SST (°C), **(b)** SSS (no unit), **(c)** NO_3 (µmol kg^{-1}), **(d)** PO_4 (µmol kg^{-1}), **(e)** SiO_4 (µmol kg^{-1}) and **(f)** pCO_2 (µatm). Observational datasets are as follows: SST and SSS are from the NOAA OI SST V2 (Reynolds et al., 2007) and the EN4 SSS (Good et al., 2013), nutrients are from the World Ocean Atlas 2018 (Garcia et al., 2019), and pCO_2 is from the coastal SOM-FFN product (Laruelle et al., 2017). Colors correspond to the seven major MARCATS classes (see Fig. 1b). In panels **(d)** and **(e)**, the Black Sea (M21) is not represented and has xy coordinates of (0.2; 3.5 µmol kg^{-1}) in panel **(d)** and (10.3; 83.1 µmol kg^{-1}) in panel **(e)**. The Antarctic shelf (M45) is also not represented in panel **(e)** (55.0;49.1 µmol kg^{-1}).

discrepancies (Fig. 4e) are found at high latitudes (poleward of 60° N and 60° S, negative bias), along the Peruvian and Namibian upwelling systems (high positive bias) and more locally close to the mouth of some large rivers (e.g., the plume of the Amazon or the Rio de la Plata, high negative bias). We note, however, that these regions are poorly sampled in the SOCATv6 dataset (Fig. 4b) and are thus likely weakly constrained in the coastal SOM-FFN product (Fig. 4d).

At the regional scale, differences in annual mean pCO_2 between MOM6-COBALT and coastal SOM-FFN are lower than 20 µatm in 35 MARCATS (Table S1, Fig. 3f), which partly is a reflection of the low annual mean biases observed in the environmental driver variables in these regions (see Sect. 3.1.1). In EBC, WBC and subpolar coastal regions, the model tends to overestimate the regional mean pCO_2 compared to coastal SOM-FFN (positive bias), except along the US East Coast (M10), in the East China Sea and Kuroshio (M39), and in the NE Atlantic (M17, Table S1). In polar regions, the model generally underestimates the mean pCO_2 compared to coastal SOM-FFN, except around S Greenland (M15). In Indian, marginal, and tropical coastal regions, no general trend can be identified regarding the sign of the bias, which can be positive or negative.

Quantitatively, the 10 MARCATS regions with absolute biases > 20 µatm are mainly located in regions for which very limited or no observational data have been compiled in the SOCATv6 database (Table S1) and/or for which large discrepancies can already be identified at the level of the master environmental variables (Sect. 3.1.1). These regions mainly belong to EBCs (three out of the six EBC MARCATS regions) and marginal seas (three out of the nine marginal seas MARCATS regions), with the remaining four being either polar (the Canadian Archipelago, M13, and the N Greenland, M14), subpolar (NW Pacific, M42) or Indian margins (the Bay of Bengal, M31). The largest biases are found in the Peruvian Upwelling Current (M4), SW Africa (M24), the Californian Upwelling Current (M2) and the Canadian Archipelago (M13), with biases of 106, 79, 35 and −53 µatm, respectively.

Our analysis reveals that the seasonal amplitudes simulated by MOM6-COBALT are systematically larger than the ones estimated by the coastal SOM-FFN product (Fig. 5a–b, red colors in Fig. 5c and positive biases in Table S2) for all coastal regions belonging to EBC, WBC, and Indian and tropical margins. For the majority of the polar and subpolar margins and for some marginal seas, the model simulates lower seasonal pCO_2 amplitudes (blue colors in Fig. 5c and negative biases in Table S2). Quantitatively, absolute biases between the modeled and coastal SOM-FFN amplitudes do not exceed 20 µatm, except for in marginal seas where larger discrepancies are calculated (six of the nine marginal MARCATS regions, Table S2). The monthly mean pCO_2 seasonal cycle simulated by MOM6-COBALT is also well in phase (Pearson correlation coefficients > 0.5) with the one extracted from coastal SOM-FFN in 34 out of the 45 MARCATS regions (Fig. 5d and Table S2). The agreement is especially good in the best-monitored MARCATS regions (MARCATS where > 50 % of the area is covered by SOCATv6 observations, Table S1). For instance, in regions with good data coverage, such as along the US East Coast (M10), the Norwegian Basin (M16), the Californian Current (M2), the Leeuwin Current (M33) or the Brazilian Current (M6), the Pearson correlation coefficient is higher than 0.9 (Ta-

ble S2). In contrast, the seasonal pCO_2 cycle simulated by MOM6-COBALT substantially diverges from that of the coastal SOM-FFN in four poorly monitored marginal seas and in a few of regions of EBCs, Indian margins, subpolar margins, and tropical margins (Pearson correlation coefficient < 0.5, Table S2 and Fig. 5d).

The model pCO_2 seasonal evaluation against SOCATv6 is only performed in 11 MARCATS regions, namely the Californian Current (M2), tropical E Pacific (M3), the Gulf of Mexico (M9), the US East Coast (M10), S Greenland (M15), Norwegian Basin (M16), NE Atlantic (M17), Iberian upwelling (M19), Moroccan upwelling (M22), China Sea and Kuroshio (M39), and New Zealand (M36). The modeled seasonal cycle is in good agreement with the one derived from SOCATv6 (Fig. 6b–l, Table S2) with absolute biases < 20 µatm for all of the 11 selected MARCATS and Pearson correlation coefficients close to 0.5 or higher except for the Iberian Upwelling (M19, Pearson value of 0.2) and on the New Zealand shelf (M36, value of 0.3). We did not perform the SOCATv6 model seasonal evaluation for the other MARCATS regions because the vast majority of grid cells only include data for less than 4 climatological months (Fig. 6a). However, we also evaluated the simulated pCO_2 seasonality against SOCATv6 in regions where this evaluation is not possible to be performed at the MARCATS scale. To do so, we selected four sites of smaller spatial extent than MARCATS for which we calculated climatological seasonal pCO_2 signals from the SOCATv6 dataset and compared them with the model pCO_2. These sites are located off the Antarctic Peninsula, on the Queensland Plateau in NE Australia, in coastal waters of Papua New Guinea and off Terra Nova in Antarctica (see black boxes in Fig. 6a). In those regions, the absolute biases of the seasonal amplitude between MOM6-COBALT and SOCATv6 (Fig. 6m–p) are less than 20 µatm, and the phase in the seasonal cycles presents a good agreement with a Pearson correlation coefficient value of 0.8, except for the Papua New Guinea data (value of 0.5). Note that the model SOCATv6 seasonal evaluation for Terra Nova presents a good agreement, but the MARCATS scale (Sea of Labrador, M11) evaluation to which this region belongs to reveals a low agreement, showing that a poor agreement between coastal SOM-FFN and the model does not equate to poor model skill when these regions are undersampled by SOCATv6.

3.1.3 Identifying coastal regions of high model to coastal SOM-FFN agreement

Overall, the pCO_2 spatiotemporal analysis model–data evaluation shows that out of 45 MARCATS regions, 29 have an absolute bias for their annual mean < 20 µatm when MOM6-COBALT-coastal SOM-FFN, MOM6-COBALT-SOCATv6 and coastal SOM-FFN-SOCATv6 are compared (Table S1). Together, these 29 MARCATS regions represent 65 % of the global coastal ocean surface area. For the 11 MARCATS regions that are best covered by observations (MARCATS regions where > 50 % of the surface area is covered by SOCATv6 observations, Table S1), absolute biases for the annual mean are always < 20 µatm for the three product intercomparison, except in the Californian Current (M2), in the Baltic Sea (M18) and along the NE Pacific (M1). The seasonal MOM6-COBALT against coastal SOM-FFN evaluation also reveals that 39 of the 45 MARCATS regions have pCO_2 seasonal amplitude biases < 20 µatm and that 34 MARCATS regions have a Pearson correlation coefficient > 0.5 (Table S2).

Based on this evaluation, we attribute for each MARCATS region a level of confidence in the model to coastal SOM-FFN agreement ("high", "medium" and "low"; see Table 1 and Fig. 1a). Out of the 45 MARCATS regions, 25 are labeled with high agreement, meaning that they fulfill the following criteria regarding the annual mean and the seasonality (Table 1 and dotted MARCATS regions in Fig. 1a): a bias < 20 µatm in the annual mean pCO_2 between MOM6-COBALT and coastal SOM-FFN, a bias < 20 µatm in the magnitude of the seasonal pCO_2 cycle, and a seasonal phase characterized by a Pearson correlation coefficient > 0.5. Note that the some MARCATS regions, i.e., the Siberian shelf (M43), the Antarctic shelf (M45), the NE Pacific (M1), the tropical E Atlantic (M23) and the tropical W Indian Ocean(M26), also present an annual mean pCO_2 bias < 20 µatm in the MOM6-COBALT-SOCATv6 and coastal SOM-FFN-SOCATv6 comparisons (Table S1). In addition, seven high-agreement MARCATS regions also show a data density > 50 % (this comes to 13 MARCATS regions if we lower the data coverage to > 30 %, Fig. 1a). These 7 MARCATS regions are located in contrasted coastal environments, i.e., three EBCs (Iberian upwelling, M19; Moroccan upwelling, M22; and the Leeuwin Current, M33), one WBC (US East Coast, M10), one Polar region (Norwegian Basin, M16), one subpolar region (NE Atlantic, M17) and one marginal sea (Gulf of Mexico, M9). These seven high-agreement MARCATS regions could also result from the very good correspondence between the data–model annual mean and seasonal patterns in environmental fields (Table S1 and Table S2, except M22, M33 and M9 for the nutrient phasing) and are therefore excellent potential candidates for an analysis of the processes controlling the coastal pCO_2 dynamics. A total of six additional MARCATS regions fulfill the criteria related to the seasonal pCO_2 evaluation, but they fail to fulfill the annual mean pCO_2 bias threshold of 20 µatm. These medium-agreement regions (Table 1 and dashed regions in Fig. 1a) include two EBCs (Californian Current, M2, and SW Africa, M24), one marginal sea (Sea of Okhotsk, M41), two polar regions (Canadian Archipelago, M13, and N Greenland, M14) and one subpolar region (NW Pacific, M42) shelves. The majority of marginal seas are systematically associated with large biases relating to either pCO_2 or the main environmental variables. These regions fulfill only one criterion (or none of them) regard-

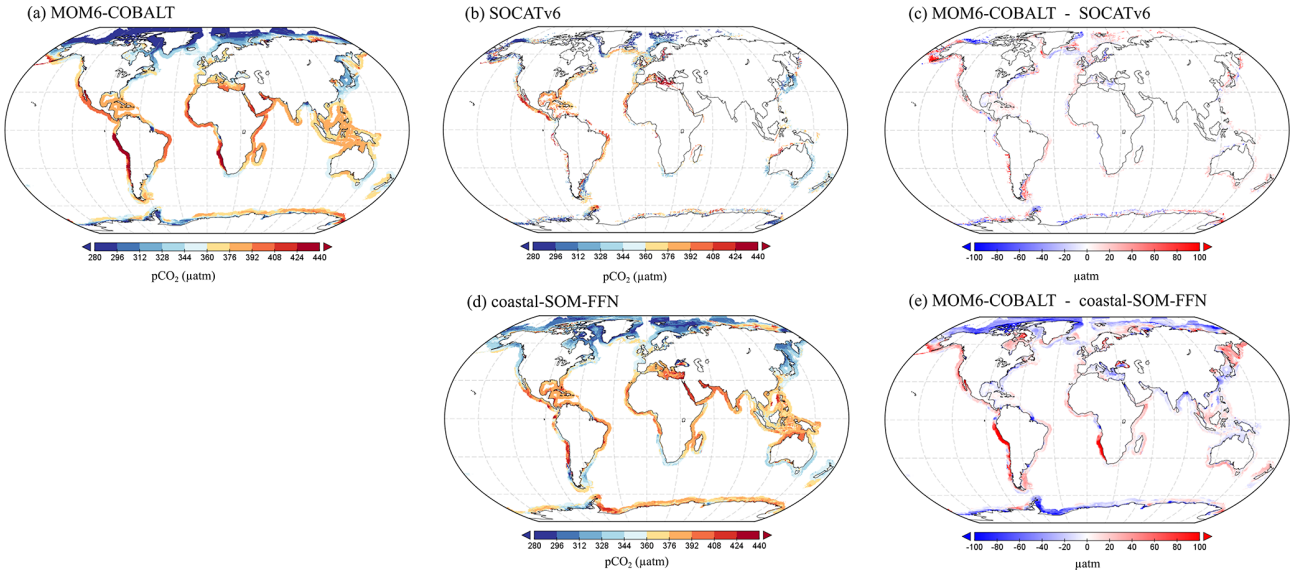

Figure 4. Spatial distributions of the annual mean pCO_2 (µatm) generated by **(a)** MOM6-COBALT and **(b)** extracted from the SOCATv6 database, **(c)** model bias given as the difference between panels **(a)** and **(b)** (in µatm; red and blue colors correspond to regions in which the pCO_2 simulated by MOM6-COBALT is higher and lower than SOCATv6, respectively). **(d)** Spatial distribution of the annual mean pCO_2 from the coastal SOM-FFN product (Laruelle et al., 2017). **(e)** Model bias given as the difference between panels **(a)** and **(d)**.

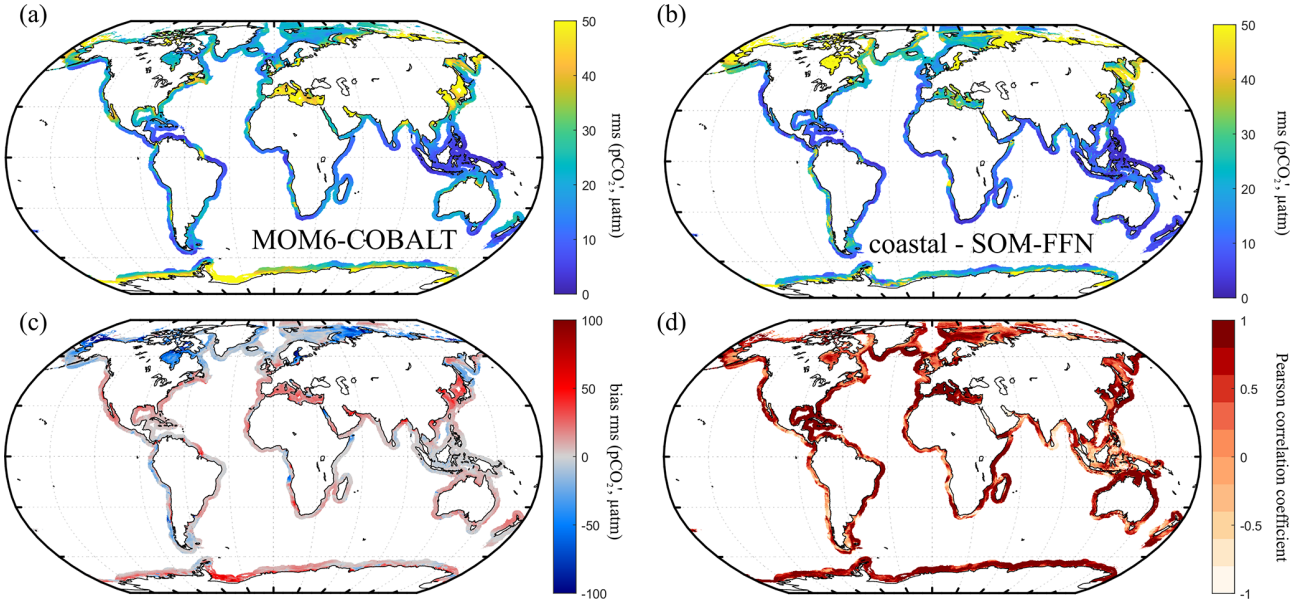

Figure 5. Seasonal variability in ocean pCO_2 (µatm). Seasonal amplitude **(a)** simulated by MOM6-COBALT model and **(b)** in the coastal SOM-FFN product, and **(c)** bias between the model and coastal SOM-FFN seasonal amplitude (red indicates that simulated amplitude exceeds coastal SOM-FFN). The seasonal amplitude is expressed as the root mean square of the monthly climatology pCO_2 anomalies ($\mathrm{rms}_{pCO_2'}$, µatm). **(d)** Pearson correlation coefficient of the regression between the seasonal pCO_2 cycles calculated by MOM6-COBALT and coastal SOM-FFN. A value of 1 indicates that both signals are perfectly in phase with one another, while a value of -1 represents a complete phase shift.

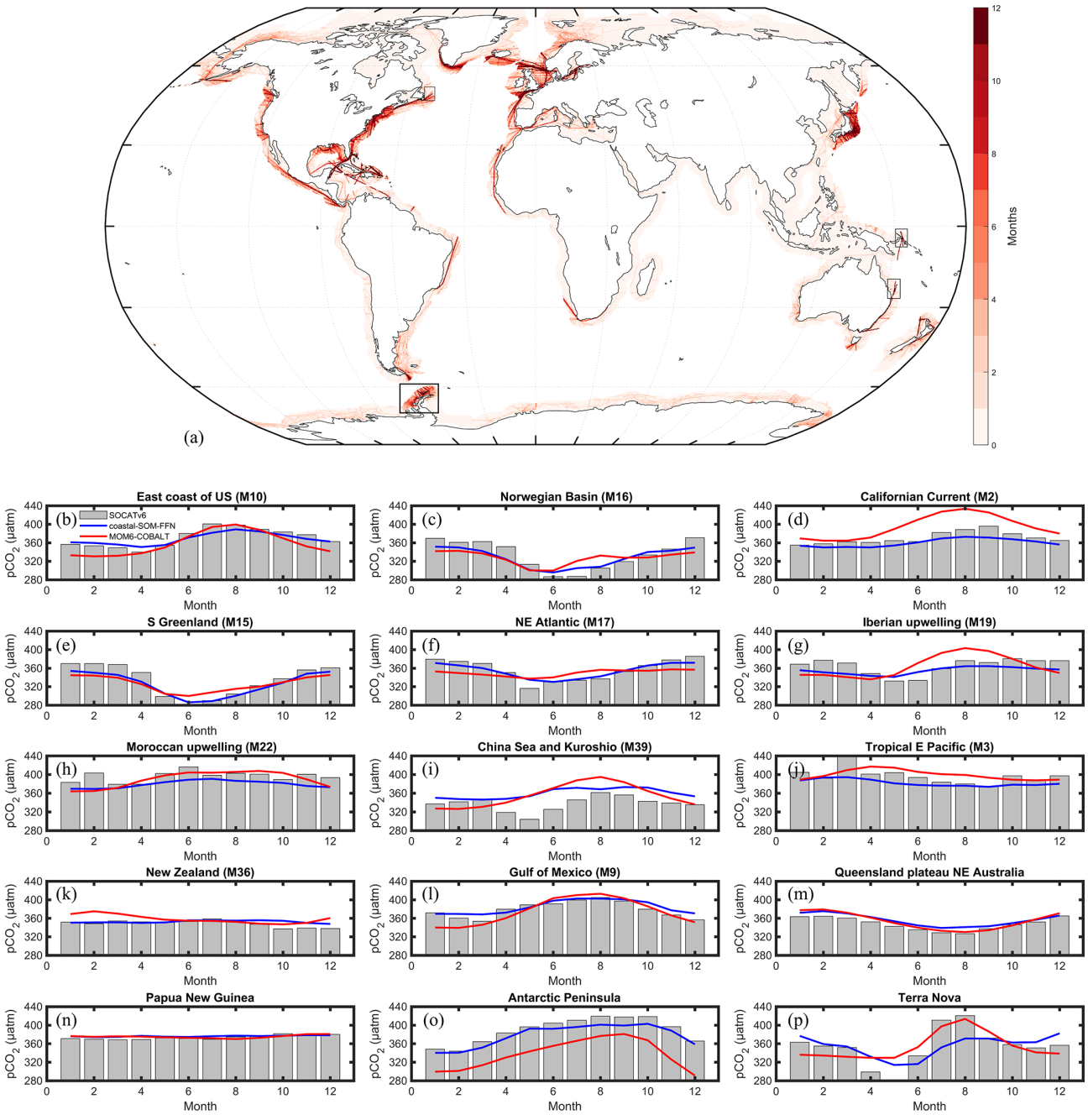

Figure 6. (a) SOCATv6 temporal coverage evaluated as the number of months (1 to 12) where at least one pCO_2 measurement is available (see details in Sect. 2). Seasonal pCO_2 cycle (µatm) derived from SOCATv6 (bar in gray) and coastal SOM-FFN (in blue) and simulated by MOM6-COBALT (in red) for several MARCATS regions **(b–l)** and four coastal sites of smaller spatial extent than a MARCATS region **(m–p)**. The location of the four coastal sites is represented by black boxes in panel **(a)**. Month 1 corresponds to January. For consistency in the *y* axis between panels, the value of 276 µatm is not represented in panel **(p)** for month 5 for the SOCATv6 data.

ing the pCO_2 seasonality, and they are hence labeled as low-agreement regions (Table 1, Fig. 1a). Other low-agreement regions include one EBC (Peruvian Upwelling Current, M4), one Indian region (Bay of Bengal, M31), two tropical regions (tropical E Pacific, M3, and SE Asia, M38), two subpolar regions (Sea of Labrador, M11, and New Zealand, M36) and one WBC region (Brazilian Current, M6).

3.1.4 Methodological limitations

While our results show a relatively good agreement between MOM6-COBALT and coastal SOM-FFN regarding the spatial and temporal pCO_2 distribution over the global coastal ocean, the comparison remains challenging for several reasons.

First, while the climatology of Laruelle et al. (2017, coastal SOM-FFN) is currently the best available product for a model–data comparison, it has its own limitations. For instance, in some regions, particularly for coastal upwellings such as the Moroccan (M22) and Peruvian (M4) upwellings, the pCO_2 fields generated by the coastal SOM-FFN do not reproduce the high and variable pCO_2 values measured in situ well (see, e.g., Friederich et al., 2008; McGregor et al., 2007). Such poor performance of the coastal SOM-FFN algorithm in these types of systems has already been identified by Laruelle et al. (2017). Indeed, upwelling regions are still relatively poorly monitored and expand partly beyond the coastal domain used by Laruelle et al. (2017), leading to locally skewed calibration of the SOM-FFN. Deficiencies in the observation-based product can thus partly explain the large model–data bias (106 µatm, the largest of all MARCATS regions) calculated in the Peruvian upwelling region. Moreover, although the Surface Ocean CO_2 Atlas database (SOCAT) has expanded significantly over the past few years, some regions are still poorly monitored. In the coastal regions where no observational data exist (e.g., in the Black Sea, the Sea of Okhotsk, the Bay of Bengal, Fig. 4b) in the SOCAT database used here (SOCATv6, Bakker et al., 2016), it is difficult to evaluate the performance of the SOM-FFN and thus of an Oceanic General Circulation Model (OGCM) in reproducing the pCO_2 field. In addition, for certain regions subjected to complex dynamic biogeochemical settings (e.g., upwelling, seasonal cover of sea ice, influenced by rivers, marginal seas), the pCO_2 field reconstructed by the SOM-FFN suffers from poor performance, which can partly be explained by the lack of observational data. This lack of observations could partly explain why MOM6-COBALT-coastal SOM-FFN pCO_2 biases exceed 20 µatm in these regions. The seasonal model evaluation against SOCATv6 is limited at the MARCATS scale and mainly performed against coastal SOM-FFN due to the very few coastal regions that contain a continuous climatological seasonal pCO_2 cycle (Fig. 6a) in the SOCATv6 database. This study highlights the regions (Fig. 1a, e.g., Indian ocean margins, the Peruvian upwelling, marginal seas) where new observational data are most urgently needed, specifically those collected during periods of the year that are currently not covered, to improve our understanding of the CO_2 exchange between coastal regions and the atmosphere at the regional and global scales. In addition, only one global continuous pCO_2 climatology derived by the SOM-FFN method currently exists for the coastal ocean. It would therefore be beneficial for the community to develop other observation-based climatologies relying on other interpolation techniques, as is currently the case for the open ocean.

Second, the model–data comparison should also be analyzed in the light of the current limitations in the model itself. OGCMs have been designed for global ocean applications, and the coarse spatial resolution of these models, on the order of 0.5° in the present study, cannot accurately resolve mesoscale and sub-mesoscale processes and tidal mixing in shelf regions even with a model configuration including parameterizations for these processes. The coastal currents are also not always well resolved because of the coarse resolution of the shelf bathymetry. These small-scale hydrodynamic features are known to affect the spatiotemporal variability of pCO_2 and the air–sea CO_2 exchange (Bourgeois et al., 2016; Kelley et al., 1971; Lachkar et al., 2007; Laruelle et al., 2010). Therefore, although MOM6-COBALT runs at 0.5°, discrepancies between coastal SOM-FFN and MOM6-COBALT in narrow EBCs such as the Peruvian Upwelling Current (M4) and along SW Africa (M33) could also be explained by the limited spatial resolution of the model. Moreover, OGCMs such as MOM6-COBALT have a relatively simple representation of biogeochemistry that does not fully capture some of the important processes of the carbon dynamics in coastal waters, such as sea ice temporal dynamics (Adcroft et al., 2019), neritic calcification (O'Mara and Dunne, 2019), or terrestrial and marine organic matter decomposition and burial (Lacroix et al., 2021a, b). Moreover, the largest biases observed in marginal seas can partly be explained by large fluvial inputs and oceanic water flows through fine-scale topography (e.g., straits) that are poorly represented in global OGCMs.

Finally, the annual mean and seasonal pCO_2 biases between the coastal SOM-FFN and MOM6-COBALT can also be traced back to divergences in the environmental fields simulated by the model compared to observations (Tables S1 and S2). For instance, in most marginal seas, the model poorly resolves the annual mean and seasonal cycle of SSS and nutrients compared to the observations. These discrepancies impact the simulated pCO_2 via the controls of the SSS on the CO_2 solubility and of nutrients on the biological pump and CO_2 uptake. In the tropical W Atlantic (M7), which is under the influence of the Amazon River, the model simulates lower annual mean SSS (and therefore lower pCO_2) than the observations. In the tropical E Pacific (M3) and in Southeast Asia (M38), the poor agreement between simulated and observed seasonal pCO_2 cycle could be explained by significant biases in the nutrient seasonal cycles (low Pearson cor-

relation coefficient). Interestingly, some regions reveal significant biases in the major environmental fields but not in the pCO_2 (e.g., the tropical W Atlantic, M7), while in other regions the reverse is observed (e.g., the Mediterranean Sea, M20; W Arabian Sea, M27; and in New Zealand, M36). In addition, for some regions biases in environmental fields do not affect the pCO_2 as expected. For instance, along the US East Coast (M10), MOM6-COBALT simulates larger SST compared to observations, while the simulated pCO_2 is lower compared to coastal SOM-FFN on an annual mean. This clearly shows that biases in environmental fields are not sufficient to fully explain the biases in pCO_2 diagnosed between MOM6-COBALT and coastal SOM-FFN.

3.2 Processes governing the seasonal pCO_2 variability

Our second objective is to examine the drivers of the pCO_2 seasonality in three well-sampled and contrasted coastal regions where the model to coastal SOM-FFN agreement is satisfactory: the US East Coast (M10), the Norwegian Basin (M16) and the Californian Current (M2). The US East Coast is a sink of atmospheric CO_2 that has been extensively studied over the past decade (e.g., Fennel et al., 2019; Laruelle et al., 2015; Shadwick et al., 2010, 2011; Signorini et al., 2013). The pCO_2 spatiotemporal dynamics in this MARCATS region are particularly well captured by MOM6-COBALT (high agreement, Fig. 1a), despite an annual mean SST bias of 1.3 °C in the data–model comparison in this region (Table S1). Because the SST amplitude and seasonal phasing are in agreement between the model and data (Table S2), the bias in the mean SST does not impact the seasonal pCO_2 cycle (Pearson correlation coefficient > 0.5 and bias < 20 µatm in the seasonal pCO_2 amplitude, Table 1). We also selected the Californian Current because it is a source of CO_2 to the atmosphere and because, similar to the US East Coast, it ranks among one of the best-monitored coastal regions in the world (e.g., Evans et al., 2011; Fennel et al., 2019; Hales et al., 2012; Turi et al., 2014). In this region, the model is classified as medium agreement (Table 1 and Fig. 1a). Indeed, the simulated seasonal cycle of pCO_2 is in relatively good agreement with coastal SOM-FFN (Figs. 5–6, and Table 1) despite biases in the annual mean pCO_2 compared to observations (Fig. 3f) and a phase shift in the seasonality of SSS and nutrients (Pearson correlation coefficient < 0.5). However, the Californian Current is also one of the few coastal regions where an analysis of the processes controlling the pCO_2 seasonality has already been performed using a regional biogeochemical model and sequential simulation removing processes one after the other (Turi et al., 2014), which can hence be compared to our analysis. Finally, the choice of the Norwegian Basin is motivated by the good performance (high agreement) of the model and the intense atmospheric CO_2 sink that occurs in this contrasted region.

3.2.1 Seasonality along the US East Coast

The seasonal evolution of pCO_2 averaged over the US East Coast (M10) is represented in Fig. 7a. Ocean pCO_2 is at a minimum in winter (February–March ~ 331 µatm), increases through spring and peaks in summer (August, ~ 400 µatm) before decreasing again in autumn. Figure 7b reveals the complex interplay of the four ocean internal processes (thermal and biological processes, ocean circulation, and freshwater flux) on the seasonal pCO_2 variability that can either act in synergy or oppose each other.

The thermal effect (thermal, red line in Fig. 7b) increases pCO_2 from early spring to summer by decreasing the solubility of CO_2. In contrast, the solubility of CO_2 increases in autumn and winter, inducing a decline in pCO_2. The largest changes in pCO_2 associated with the change in SST occur during spring (29 µatm per month in June) and autumn (-26 µatm per month in November). This thermal effect was already identified by Signorini et al. (2013) in their observational study and further confirmed by Cai et al. (2020). These authors highlighted that lowest pCO_2 was generally reported in winter or at the beginning of spring and highest pCO_2 in summer or autumn, despite significant temporal and spatial heterogeneity between the different sub-regions of the US East Coast (Scotian shelf, the Gulf of Maine, the Georges Bank and Nantucket shoals, the Middle Atlantic Bight, and the South Atlantic Bight). The effect of biological processes above the mixed-layer depth (bio, green line) reduces pCO_2 throughout the year, revealing that primary production exceeds organic matter degradation in the surface layer all year long. The largest pCO_2 decrease associated with biological processes is observed in early spring (values of -68 µatm per month in April), which is well documented (e.g., Shadwick et al., 2010, 2011; Signorini et al., 2013). The transport of chemical species by ocean circulation (circ, blue line) increases pCO_2 and tends to oppose biological processes year-round except at the end of autumn and beginning of winter. This pCO_2 increase induced by the circulation term is at its maximum in April (26 µatm per month). Throughout the year, the contribution of freshwater fluxes (fw, pink line) remains minor compared to the other terms (maximum absolute value of 9 µatm per month in January). For each month and season, the air–sea CO_2 exchange term (CO_2 flux, black line) counteracts change in pCO_2 associated with ocean internal processes taking place in surface seawater (sum of bio, circ, thermal and fw). The CO_2 flux term increases pCO_2 at the sea surface (acting as an atmospheric CO_2 sink) throughout the year, except during summer (between July and September) where it decreases sea surface pCO_2 and releases CO_2 towards the atmosphere (acting as an atmospheric CO_2 source). This year-round simulated atmospheric CO_2 uptake (except for the summer season) is also in agreement with previous literature (Fennel et al., 2019; Laruelle et al., 2015; Signorini et al., 2013). The study of Laruelle et al. (2015) has nevertheless shown that

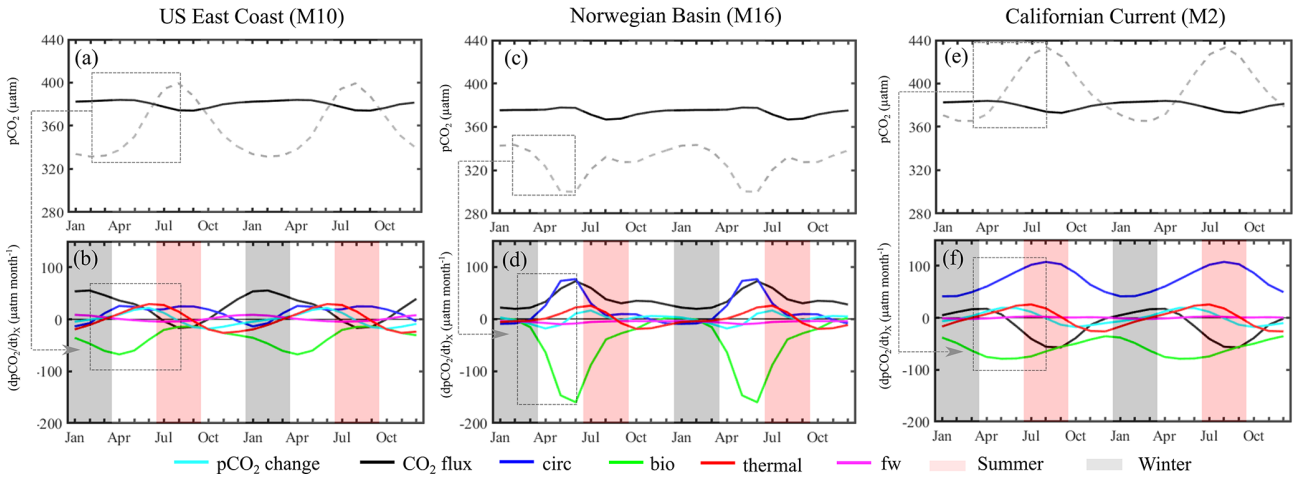

Figure 7. Processes controlling the ocean pCO_2 seasonal cycle. Mean seasonal sea surface pCO_2 (dashed line) and atmospheric pCO_2 (black line; in µatm) simulated by MOM6-COBALT and detrended over **(a)** the US East Coast (M10), **(c)** the Norwegian sea (M16) and **(e)** the Californian current (M2). Spatially averaged contributions (in µatm month^{-1}) from biological activity (bio, green), temperature changes (thermal, red), transport of chemical species (circ, blue), freshwater flux (fw, pink) and the CO_2 air–sea flux (CO_2 flux, black) controlling the pCO_2 temporal change (pCO_2 change, cyan) for the three regions (**b**, **d**, **f**). A positive value corresponds to an increase in sea surface pCO_2. Winter corresponds to the months of January, February and March, and summer corresponds to the months of July, August and September.

in spring the southern part of the US East Coast is quasi-neutral and that in autumn some regions, such as the Gulf of Maine or the Georges Bank, act as a CO_2 source. The temporal change of pCO_2 (pCO_2 change, cyan line) is the result of the non-perfect balance between the internal processes and the air–sea CO_2 flux.

We evaluate the rate of change tied to each process during the marked peak-to-peak pCO_2 increase observed between winter and summer (from 331 µatm in February to 400 µatm in August, Fig. 7a). A positive rate of change (in µatm per month) indicates that the process contributes to an increase in pCO_2 between winter and summer (February–August). This process-based analysis reveals that the winter-to-summer pCO_2 increase on the US East Coast (M10) mainly results from thermal (rate of change $= +5$ µatm per month) and ocean circulation (rate of change $= +4$ µatm per month) influences combined with a large reduction of the biological CO_2 uptake (rate change of $+7$ µatm per month, Fig. 7b). The importance of the thermal and circulation effects and the presence of a strong biological drawdown are in line with results from past studies (e.g., Laruelle et al., 2015; Shadwick et al., 2010, 2011; Signorini et al., 2013; and Cai et al., 2020). Our results identify the reduction of biological carbon uptake as a key control of pCO_2 seasonality and thus agree with the studies of Shadwick et al. (2010, 2011) but slightly diverge compared to those of Signorini et al. (2013) or Laruelle et al. (2015), which found that the thermal effect was the dominant driver. This difference is largely explained by the different levels of details in the decomposition method. While most model studies, including ours, use seasonal change in SST, SSS, DIC and ALK, observational approaches cannot isolate the compounding changes tied to biological activity from those of ocean transport.

3.2.2 Seasonality in the Norwegian basin and in the Californian Current

The pCO_2 seasonal cycle in the Norwegian Basin (M16) and the Californian Current (M2) simulated by MOM6-COBALT are represented in Fig. 7c and e, respectively. The Norwegian Basin shows a near-constant pCO_2 value ($\sim$330 µatm) throughout the year, except in spring when it drops by 30 µatm (minimum pCO_2 value of 300 µatm in June). The phasing of the seasonal pCO_2 cycle in the Californian Current is similar to that along the US East Coast, with a minimum pCO_2 value of 366 µatm in March followed by an increase that reaches a maximum pCO_2 value of 433 µatm in August and then decreases again at the beginning of autumn.

The decomposition of the seasonal cycle into different processes for both the Norwegian Basin and the Californian Current (Fig. 7d and f) reveal patterns that are qualitatively similar to those already diagnosed for the US East Coast (Fig. 7b). For both shelf regions, the biological and circulation effects remain negative and positive, respectively, throughout the year, while the thermal effect increases pCO_2 in spring and summer but decreases pCO_2 in autumn and winter. The freshwater term is also minor compared to the other terms. Quantitatively, however, the amplitude of the different terms points to different first-order control in the pCO_2 seasonality for each region. The amplitudes are calculated here using the marked peak-to-peak change in pCO_2, which occurs between February and June in the Norwegian

basin and between March and August in the Californian Current.

In the Norwegian basin, the strong winter to summer pCO_2 decreases (43 µatm, Fig. 7c) are mainly associated with the large and rapid CO_2 uptake associated with the spring phytoplankton bloom (biological rate of change = −45 µatm per month on average between February and June, with a maximum pCO_2 uptake of −175 µatm per month in June, Fig. 7d). This biological drawdown is only partly compensated for by the supply of high pCO_2 water masses from the ocean circulation (rate of change = +24 µatm per month). These dynamics are consistent with the fact that the Norwegian Basin is one of the most productive regions of the world and is characterized by a well-documented, intense spring bloom (e.g., Findlay et al., 2008). In addition, the effect of thermal changes only plays a comparatively minor role here (rate of change = +7 µatm per month).

In contrast to the US East Coast and the Norwegian Basin, the analysis performed in the Californian Current reveals that circulation is the main driver of the winter-to-summer pCO_2 increases (68 µatm, Fig. 7e). The upwelling of high-pCO_2 waters increases year-round surface pCO_2. However, its influence is weaker in winter than in summer, thereby explaining the pCO_2 increase observed between February and August (rate of change = +12 µatm per month, Fig. 7f). This large contribution from circulation is consistent with the simulations of Turi et al. (2014), who identified the ocean transport associated with upwelling in the Californian Current as the dominant process, and the higher intensity of the summer upwelling and its impact on pCO_2 were also reported in prior work (e.g., Evans et al., 2015; Fiechter et al., 2014; Turi et al., 2014). In this region, biological processes also oppose the effect of ocean circulation, with upwelled deep water bringing nutrients to the surface and stimulating phytoplankton productivity (e.g., Evans et al., 2015; Fiechter et al., 2014; Turi et al., 2014). However, it plays a minor role in the pCO_2 increase (rate of change ∼ 0 µatm per month) and the thermal effect (rate of change = +4 µatm per month).

4 Conclusions

In this study, an OGCM (MOM6-COBALT) that is primarily designed for the open ocean was used to examine sea surface pCO_2 seasonality in the coastal domain. We first evaluated the ability of the model to reproduce the spatial and temporal dynamics of key environmental variables, such as SST, SSS and sea surface nutrients, against in situ observations. The spatiotemporal variability of coastal pCO_2 was also evaluated using direct coastal pCO_2 observations from the SOCAT database (SOCATv6, Bakker et al., 2016) and a global observational continuous monthly pCO_2 climatology available at high spatial resolution (coastal SOM-FFN, Laruelle et al., 2017).

Our model–data comparison showed a relatively good agreement on the environmental variables spatiotemporal distribution except for some coastal regions mainly located in marginal seas. Our results also revealed a relatively good agreement, both in time and space, between pCO_2 from MOM6-COBALT, coastal SOM-FFN and SOCATv6, and most of the discrepancies between the three products are found in regions with poor data coverage, such as in the Bay of Bengal, the Sea of Okhotsk or Hudson Bay (Fig. 1a). This study highlights the regions (Fig. 1a, e.g., Indian Ocean margins, Peruvian upwelling, marginal seas) where new observational data are most urgently needed, specifically data collected during different periods of the year that are currently missing to improve our understanding of the CO_2 exchange between coastal regions and the atmosphere at the regional and global scales. From the model–data evaluation, we identified regions where the MOM6-COBALT model shows the highest agreement in reproducing the spatial and seasonal pCO_2 variability, and where the different processes governing the pCO_2 dynamics can be examined with reasonable confidence (high- and medium-agreement regions in Table 1 and Fig. 1a).

We also adapted a novel method to quantify the contributions of the different physical and biological processes governing the sea surface pCO_2 seasonality in the coastal domain. This method goes one step further than past coastal studies (e.g., Signorini et al., 2013; Turi et al., 2014) where the processes attribution was only based on the seasonal changes in DIC, ALK, SST and SSS and/or combined with a series of sequential simulations isolating one term after the other. In particular, our simulations are non-sequential and allow us to account for the co-variations between the different variables impacted by each process and how their simultaneous evolution modulates pCO_2 dynamics in quantitative terms. Our approach, which is illustrated in three coastal regions (the US East Coast, the California Current and the Norwegian Basin), allows to decipher the complex interplay between ocean transport of chemical species (DIC, ALK and SSS), biological drawdown, freshwater fluxes (dilution and concentration effects) and thermal changes (air–sea fluxes and transport of temperature) on the pCO_2 dynamics. Depending on the season and region, these terms can reinforce or oppose each other and act to strengthen or dampen the amplitude of pCO_2 seasonal variations that control the air–sea CO_2 exchange. Along the US East Coast and in the Californian Current, pCO_2 increases from winter to summer. In the former region, this increase is controlled by a subtle balance between biological drawdown, thermal changes and ocean circulation, while in the Californian Current the circulation due to the upwelling (supplying pCO_2-rich waters to the surface) drives the increase in pCO_2. In contrast, in the Norwegian Basin biological drawdown dominates the marked spring pCO_2 decrease observed in the region. These differences in the quantitative controls of pCO_2 dynamics from one region to another support our proposed analysis at

the broad scale of the 45 MARCATS regions that together compose the global coastal ocean.

A handful of observation-based studies have analyzed the seasonal variability of pCO_2 in the global coastal ocean (Cao et al., 2020; Chen and Hu, 2019; Laruelle et al., 2017). The mechanistic understanding of seasonal pCO_2 variations was and remains limited by the amount of available observations. The modeling approach tailored for the coastal ocean presented in this paper complements observational studies and helps to improve our quantitative understanding of the underlying physical and biological drivers of coastal pCO_2 dynamics. The comparison of the model performance to a state-of-the-art coastal pCO_2 database and continuous pCO_2 data product also lends confidence to our model results for a large fraction of the global coastal domain. The coastal ocean is under tremendous anthropogenic pressure (e.g., climate, land-use change, agriculture, pollution, urbanization; see, e.g., Mackenzie et al., 2005; Regnier et al., 2013; Seitzinger et al., 2005). Understanding the interplay between physical, biological and thermal processes and how they control coastal pCO_2 worldwide will be key to assessing how their future changes impact air–sea CO_2 exchange in coastal environments.

Data availability. The Surface Ocean CO_2 Atlas (SOCAT) is an international effort, endorsed by the International Ocean Carbon Coordination Project (IOCCP), the Surface Ocean Lower Atmosphere Study (SOLAS) and the Integrated Marine Biosphere Research (IMBeR) program, to deliver a uniformly quality-controlled surface ocean CO_2 database. The many researchers and funding agencies responsible for the collection of data and quality control are thanked for their contributions to SOCAT. Every previous version of the SOCAT database can also be accessed from the following page: https://www.socat.info/index.php/previous-versions/, last access: October 2021 (Bakker et al., 2016). The coastal SOM-FFN pCO_2 dataset description and dataset can be downloaded from https://doi.org/10.5194/bg-14-4545-2017-supplement (Laruelle et al., 2017), and the atmospheric CO_2 concentration data (xCO_2) can be derived from the Earth System Research Laboratory, available at: https://www.esrl.noaa.gov/gmd/ccgg/mbl/ (last access: March 2021) (Conway et al., 1994) and https://doi.org/10.3334/ORNLDAAC/1111 (Masarie, 2012). The SST and SSS used for the evaluation the model were extracted from the NOAA OI SST V2, available at: https://psl.noaa.gov/data/gridded/data.noaa.oisst.v2.highres.html (last access: March 2021) (Reynolds et al., 2007) and the EN4 SSS, available at: https://www.metoffice.gov.uk/hadobs/en4/ (last access: March 2021) (Good et al., 2013), respectively. Nutrients data were extracted from the World Ocean Atlas 2018, available at: https://www.ncei.noaa.gov/products/world-ocean-atlas (last access: June 2021) (Garcia et al., 2019). The delineation and description of the MARCATS segmentation can be found in Laruelle et al. (2013).

Supplement. The supplement related to this article is available online at: https://doi.org/10.5194/os-18-67-2022-supplement.

Author contributions. AR, LR and GGL designed the study. EL performed all the MOM6-COBALT simulations and implemented the changes in the model. AR, LR and PR prepared the manuscript, with contributions from all co-authors.

Competing interests. The contact author has declared that neither they nor their co-authors have any competing interests.

Disclaimer. Publisher's note: Copernicus Publications remains neutral with regard to jurisdictional claims in published maps and institutional affiliations.

Acknowledgements. We thank the two anonymous reviewers and the *Ocean Science* editor Mario Hoppema for their constructive comments. We thank the MOM6 ocean model development team and are grateful to David Luet and the Princeton Institute for Computational Science and Engineering (PICSciE) for their help and technical support for running the ocean model MOM6 at Princeton University. Goulven G. Laruelle is research associate of the F.R.S-FNRS at the Université Libre de Bruxelles.

Financial support. This research received financial support from BELSPO through the project ReCAP, which is part of the Belgian research program FedTwin, and from the European Union's Horizon 2020 research and innovation program VERIFY (grant no. 776810) and ESM 2025 – Earth System Models for the Future (grant no. 101003536) projects. Laure Resplandy and Enhui Liao acknowledge the Cooperative Institute for Modeling the Earth System between NOAA GFDL and Princeton University, the Sloan Research foundation, and the Princeton Catalysis Initiative.

Review statement. This paper was edited by Mario Hoppema and reviewed by two anonymous referees.

References

Adcroft, A., Anderson, W., Balaji, V., Blanton, C., Bushuk, M., Dufour, C. O., Dunne, J. P., Griffies, S. M., Hallberg, R., Harrison, M. J., Held, I. M., Jansen, M. F., John, J. G., Krasting, J. P., Langenhorst, A. R., Legg, S., Liang, Z., McHugh, C., Radhakrishnan, A., Reichl, B. G., Rosati, T., Samuels, B. L., Shao, A., Stouffer, R., Winton, M., Wittenberg, A. T., Xiang, B., Zadeh, N., and Zhang, R.: The GFDL Global Ocean and Sea Ice Model OM4.0: Model Description and Simulation Features, J. Adv. Model. Earth Sy., 11, 3167–3211, https://doi.org/10.1029/2019MS001726, 2019.

Arruda, R., Calil, P. H. R., Bianchi, A. A., Doney, S. C., Gruber, N., Lima, I., and Turi, G.: Air-sea CO_2 fluxes and the controls on ocean surface pCO_2 seasonal variability in the coastal and open-ocean southwestern Atlantic Ocean: a modeling study, Biogeosciences, 12, 5793–5809, https://doi.org/10.5194/bg-12-5793-2015, 2015.

Bakker, D. C. E., Pfeil, B., Landa, C. S., Metzl, N., O'Brien, K. M., Olsen, A., Smith, K., Cosca, C., Harasawa, S., Jones, S. D., Nakaoka, S., Nojiri, Y., Schuster, U., Steinhoff, T., Sweeney, C., Takahashi, T., Tilbrook, B., Wada, C., Wanninkhof, R., Alin, S. R., Balestrini, C. F., Barbero, L., Bates, N. R., Bianchi, A. A., Bonou, F., Boutin, J., Bozec, Y., Burger, E. F., Cai, W.-J., Castle, R. D., Chen, L., Chierici, M., Currie, K., Evans, W., Featherstone, C., Feely, R. A., Fransson, A., Goyet, C., Greenwood, N., Gregor, L., Hankin, S., Hardman-Mountford, N. J., Harlay, J., Hauck, J., Hoppema, M., Humphreys, M. P., Hunt, C. W., Huss, B., Ibánhez, J. S. P., Johannessen, T., Keeling, R., Kitidis, V., Körtzinger, A., Kozyr, A., Krasakopoulou, E., Kuwata, A., Landschützer, P., Lauvset, S. K., Lefèvre, N., Lo Monaco, C., Manke, A., Mathis, J. T., Merlivat, L., Millero, F. J., Monteiro, P. M. S., Munro, D. R., Murata, A., Newberger, T., Omar, A. M., Ono, T., Paterson, K., Pearce, D., Pierrot, D., Robbins, L. L., Saito, S., Salisbury, J., Schlitzer, R., Schneider, B., Schweitzer, R., Sieger, R., Skjelvan, I., Sullivan, K. F., Sutherland, S. C., Sutton, A. J., Tadokoro, K., Telszewski, M., Tuma, M., van Heuven, S. M. A. C., Vandemark, D., Ward, B., Watson, A. J., and Xu, S.: A multi-decade record of high-quality fCO_2 data in version 3 of the Surface Ocean CO_2 Atlas (SOCAT), Earth Syst. Sci. Data, 8, 383–413, https://doi.org/10.5194/essd-8-383-2016, 2016 (data available at: https://www.socat.info/index.php/previous-versions/, last access: March 2021).

Borges, A. V., Delille, B., and Frankignoulle, M.: Budgeting sinks and sources of CO_2 in the coastal ocean: Diversity of ecosystem counts, Geophys. Res. Lett., 32, 1–4, https://doi.org/10.1029/2005GL023053, 2005.

Bourgeois, T., Orr, J. C., Resplandy, L., Terhaar, J., Ethé, C., Gehlen, M., and Bopp, L.: Coastal-ocean uptake of anthropogenic carbon, Biogeosciences, 13, 4167–4185, https://doi.org/10.5194/bg-13-4167-2016, 2016.

Cai, W.-J.: Estuarine and Coastal Ocean Carbon Paradox: CO_2 Sinks or Sites of Terrestrial Carbon Incineration?, Ann. Rev. Mar. Sci., 3, 123–145, https://doi.org/10.1146/annurev-marine-120709-142723, 2011.

Cai, W.-J., Xu, Y.-Y., Feely, R. A., Wanninkhof, R., Jönsson, B., Alin, S. R., Barbero, L., Cross, J. N., Azetsu-Scott, K., Fassbender, A. J., Carter, B. R., Jiang, L.-Q., Pepin, P., Chen, B., Hussain, N., Reimer, J. J., Xue, L., Salisbury, J. E., Hernández-Ayón, J. M., Langdon, C., Li, Q., Sutton, A. J., Chen, C.-T. A., and Gledhill, D. K.: Controls on surface water carbonate chemistry along North American ocean margins, Nat. Commun., 11, 1–13, https://doi.org/10.1038/s41467-020-16530-z, 2020.

Cao, Z., Yang, W., Zhao, Y., Guo, X., Yin, Z., Du, C., Zhao, H., and Dai, M.: Diagnosis of CO_2 dynamics and fluxes in global coastal oceans, Natl. Sci. Rev., 7, 786–797, https://doi.org/10.1093/nsr/nwz105, 2020.

Chen, S. and Hu, C.: Environmental controls of surface water pCO_2 in different coastal environments: Observations from marine buoys, Cont. Shelf Res., 183, 73–86, https://doi.org/10.1016/j.csr.2019.06.007, 2019.

Chen, C.-T. A., Huang, T.-H., Chen, Y.-C., Bai, Y., He, X., and Kang, Y.: Air–sea exchanges of CO_2 in the world's coastal seas, Biogeosciences, 10, 6509–6544, https://doi.org/10.5194/bg-10-6509-2013, 2013.

Conway, T. J., Tans, P. P., Waterman, L. S., Thoning, K. W., Kitzis, D. R., Masarie, K. A., and Zhang, N.: Evidence for interannual variability of the carbon cycle from the National Oceanic and Atmospheric Administration/Climate Monitoring and Diagnostics Laboratory Global Air Sampling Network, J. Geophys. Res., 99, 22831–22855, https://doi.org/10.1029/94jd01951, 1994 (data available at: https://www.esrl.noaa.gov/gmd/ccgg/mbl/, last access: March 2021).

Doney, S. C., Lima, I., Feely, R. A., Glover, D. M., Lindsay, K., Mahowald, N., Moore, J. K., and Wanninkhof, R.: Mechanisms governing interannual variability in upper-ocean inorganic carbon system and air–sea CO_2 fluxes: Physical climate and atmospheric dust, Deep Sea Res. Pt. II, 56, 640–655, https://doi.org/10.1016/j.dsr2.2008.12.006, 2009.

Egleston, E. S., Sabine, C. L., and Morel, F. M. M.: Revelle revisited: Buffer factors that quantify the response of ocean chemistry to changes in DIC and alkalinity, Global Biogeochem. Cy., 24, GB1002, https://doi.org/10.1029/2008GB003407, 2010.

Evans, W., Hales, B., and Strutton, P. G.: Seasonal cycle of surface ocean pCO_2 on the Oregon shelf, J. Geophys. Res.-Ocean., 116, C05012, https://doi.org/10.1029/2010JC006625, 2011.

Evans, W., Hales, B., Strutton, P. G., Shearman, R. K., and Barth, J. A.: Failure to bloom: Intense upwelling results in negligible phytoplankton response and prolonged CO_2 outgassing over the Oregon shelf, J. Geophys. Res.-Ocean., 120, 1446–1461, https://doi.org/10.1002/2014JC010580, 2015.

Fennel, K., Alin, S., Barbero, L., Evans, W., Bourgeois, T., Cooley, S., Dunne, J., Feely, R. A., Hernandez-Ayon, J. M., Hu, X., Lohrenz, S., Muller-Karger, F., Najjar, R., Robbins, L., Shadwick, E., Siedlecki, S., Steiner, N., Sutton, A., Turk, D., Vlahos, P., and Wang, Z. A.: Carbon cycling in the North American coastal ocean: a synthesis, Biogeosciences, 16, 1281–1304, https://doi.org/10.5194/bg-16-1281-2019, 2019.

Fiechter, J., Curchitser, E. N., Edwards, C. A., Chai, F., Goebel, N. L., and Chavez, F. P.: Air-sea CO_2 fluxes in the California Current: Impacts of model resolution and coastal topography, Global Biogeochem. Cy., 28, 371–385, https://doi.org/10.1002/2013GB004683, 2014.

Findlay, H. S., Tyrrell, T., Bellerby, R. G. J., Merico, A., and Skjelvan, I.: Carbon and nutrient mixed layer dynamics in the Norwegian Sea, Biogeosciences, 5, 1395–1410, https://doi.org/10.5194/bg-5-1395-2008, 2008.

Frankignoulle, M. and Borges, A. V.: European continental shelf as a significant sink for atmospheric carbon dioxide, Global Biogeochem. Cy., 15, 569–576, https://doi.org/10.1029/2000GB001307, 2001.

Friederich, G. E., Ledesma, J., Ulloa, O., and Chavez, F. P.: Air-sea carbon dioxide fluxes in the coastal southeastern tropical Pacific, Prog. Oceanogr., 79, 156–166, https://doi.org/10.1016/j.pocean.2008.10.001, 2008.

Friedlingstein, P., Jones, M. W., O'Sullivan, M., Andrew, R. M., Hauck, J., Peters, G. P., Peters, W., Pongratz, J., Sitch, S., Le Quéré, C., Bakker, D. C. E., Canadell, J. G., Ciais, P., Jackson, R. B., Anthoni, P., Barbero, L., Bastos, A., Bastrikov, V., Becker, M., Bopp, L., Buitenhuis, E., Chandra, N., Chevallier, F., Chini, L. P., Currie, K. I., Feely, R. A., Gehlen, M., Gilfillan, D., Gkritzalis, T., Goll, D. S., Gruber, N., Gutekunst, S., Harris, I., Haverd, V., Houghton, R. A., Hurtt, G., Ilyina, T., Jain, A. K., Joetzjer, E., Kaplan, J. O., Kato, E., Klein Goldewijk, K., Korsbakken, J. I., Landschützer, P., Lauvset, S. K., Lefèvre, N., Lenton, A., Lienert, S., Lombardozzi, D., Marland, G., McGuire,

P. C., Melton, J. R., Metzl, N., Munro, D. R., Nabel, J. E. M. S., Nakaoka, S.-I., Neill, C., Omar, A. M., Ono, T., Peregon, A., Pierrot, D., Poulter, B., Rehder, G., Resplandy, L., Robertson, E., Rödenbeck, C., Séférian, R., Schwinger, J., Smith, N., Tans, P. P., Tian, H., Tilbrook, B., Tubiello, F. N., van der Werf, G. R., Wiltshire, A. J., and Zaehle, S.: Global Carbon Budget 2019, Earth Syst. Sci. Data, 11, 1783–1838, https://doi.org/10.5194/essd-11-1783-2019, 2019.

Garcia, H. E., Locarnini, R. A., Boyer, T. P., Antonov, J. I., Baranova, O. K., Zweng, M. M., Reagan, J. R., and Johnson, D. R.: dissolved oxygen, apparent oxygen utilization, and oxygen saturation, World Ocean Atlas 2013, NOAA Atlas NESDIS 75, Volume 3, Ocean Climate Laboratory, National Oceanographic Data Center, 27 pp., https://doi.org/10.7289/V5XG9P2W, 2013a.

Garcia, H. E., Locarnini, R. A., Boyer, T. P., Antonov, J. I., Baranova, O. K., Zweng, M. M., Reagan, J. R., Johnson, D. R., and Mishonov, A. V.: Dissolved inorganic nutrients (phosphate, nitrate, silicate), World ocean atlas 2013, NOAA Atlas NESDIS 76, Volume 4, Ocean Climate Laboratory, National Oceanographic Data Center, 25 pp., https://doi.org/10.7289/V5J67DWD, 2013b.

Garcia, H. E., Weathers, K. W., Paver, C. R., Smolyar, I., Boyer, T. P., Locarnini, R. A., Zweng, M. M., Mishonov, A.V., Baranova, O.K., Seidov, D., and Reagan, J. R.: Dissolved Inorganic Nutrients (phosphate, nitrate and nitrate + nitrite, silicate), NOAA Atlas World Ocean Atlas 2018, Volume 4, available at: https://www.ncei.noaa.gov/sites/default/files/2020-04/woa18_vol4.pdf (last access: June 2021), 2019 (data available at: https://www.ncei.noaa.gov/products/world-ocean-atlas, last access: June 2021).

Good, S. A., Martin, M. J., and Rayner, N. A.: EN4: Quality controlled ocean temperature and salinity profiles and monthly objective analyses with uncertainty estimates, J. Geophys. Res.-Ocean., 118, 6704–6716, https://doi.org/10.1002/2013JC009067, 2013 (data available at: https://www.metoffice.gov.uk/hadobs/en4/, last access: March 2021).

Gruber, N., Gloor, M., Mikaloff Fletcher, S. E., Doney, S. C., Dutkiewicz, S., Follows, M. J., Gerber, M., Jacobson, A. R., Joos, F., Lindsay, K., Menemenlis, D., Mouchet, A., Müller, S. A., Sarmiento, J. L., and Takahashi, T.: Oceanic sources, sinks, and transport of atmospheric CO_2, Global Biogeochem. Cy., 23, GB1005, https://doi.org/10.1029/2008GB003349, 2009.

Gruber, N., Clement, D., Carter, B. R., Feely, R. A., Van Heuven, S., Hoppema, M., Ishii, M., Key, R. M., Kozyr, A., Lauvset, S. K., Lo Monaco, C., Mathis, J. T., Murata, A., Olsen, A., Perez, F. F., Sabine, C. L., Tanhua, T., and Wanninkhof, R.: The oceanic sink for anthropogenic CO_2 from 1994 to 2007, Science, 3, 1193–1199, https://doi.org/10.1126/science.aau5153, 2019.

Hales, B., Strutton, P. G., Saraceno, M., Letelier, R., Takahashi, T., Feely, R., Sabine, C., and Chavez, F.: Satellite-based prediction of pCO_2 in coastal waters of the eastern North Pacific, Prog. Oceanogr., 103, 1–15, https://doi.org/10.1016/j.pocean.2012.03.001, 2012.

Keeling, R. F. and Manning, A. C.: Studies of Recent Changes in Atmospheric O_2 Content, in: treatise on Geochemistry: Second Edition, vol. 5, edited by: Holland, H. D. and Turekian, K. K., Elsevier, Amsterdam, 385–404, 2014.

Kelley, J. J., Longerich, L. L., and Hood, D. W.: Effect of upwelling, mixing, and high primary productivity on CO_2 concentrations in surface waters of the Bering Sea, J. Geophys. Res., 76, 8687–8693, https://doi.org/10.1029/jc076i036p08687, 1971.

Khatiwala, S., Tanhua, T., Mikaloff Fletcher, S., Gerber, M., Doney, S. C., Graven, H. D., Gruber, N., McKinley, G. A., Murata, A., Ríos, A. F., and Sabine, C. L.: Global ocean storage of anthropogenic carbon, Biogeosciences, 10, 2169–2191, https://doi.org/10.5194/bg-10-2169-2013, 2013.

Lachkar, Z., Orr, J. C., Dutay, J. C., and Delectase, P.: Effects of mesoscale eddies on global ocean distributions of CFC-11, CO_2, and $\Delta^{14}C$, Ocean Sci., 3, 461–482, https://doi.org/10.5194/os-3-461-2007, 2007.

Lacroix, F., Ilyina, T., Mathis, M., Laruelle, G. G., and Regnier, P.: Historical increases in land-derived nutrient inputs may alleviate effects of a changing physical climate on the oceanic carbon cycle, Glob. Chang. Biol., 27, 5491–5513, https://doi.org/10.1111/gcb.15822, 2021a.

Lacroix, F., Ilyina, T., Laruelle, G. G., and Regnier, P.: Reconstructing the Preindustrial Coastal Carbon Cycle Through a Global Ocean Circulation Model: Was the Global Continental Shelf Already Both Autotrophic and a CO_2 Sink?, Global Biogeochem. Cy., 35, e2020GB006603, https://doi.org/10.1029/2020GB006603, 2021b.

Landschützer, P., Gruber, N., Bakker, D. C. E., and Schuster, U.: Recent variability of the global ocean carbon sink, Global Biogeochem. Cy., 28, 927–949, https://doi.org/10.1002/2014GB004853, 2014.

Landschützer, P., Gruber, N., Bakker, D. C. E., Stemmler, I., and Six, K. D.: Strengthening seasonal marine CO_2 variations due to increasing atmospheric CO_2, Nat. Clim. Chang., 8, 146–150, https://doi.org/10.1038/s41558-017-0057-x, 2018.

Laruelle, G. G., Dürr, H. H., Slomp, C. P., and Borges, A. V.: Evaluation of sinks and sources of CO_2 in the global coastal ocean using a spatially-explicit typology of estuaries and continental shelves, Geophys. Res. Lett., 37, 1–6, https://doi.org/10.1029/2010GL043691, 2010.

Laruelle, G. G., Dürr, H. H., Lauerwald, R., Hartmann, J., Slomp, C. P., Goossens, N., and Regnier, P.: Global multi-scale segmentation of continental and coastal waters from the watersheds to the continental margins, Hydrol. Earth Syst. Sci., 17, 2029–2051, https://doi.org/10.5194/hess-17-2029-2013, 2013.

Laruelle, G. G., Lauerwald, R., Pfeil, B., and Regnier, P.: Regionalized global budget of the CO_2 exchange at the air-water interface in continental shelf seas, Global Biogeochem. Cy., 28, 1199–1214, https://doi.org/10.1002/2014GB004832, 2014.

Laruelle, G. G., Lauerwald, R., Rotschi, J., Raymond, P. A., Hartmann, J., and Regnier, P.: Seasonal response of air–water CO_2 exchange along the land–ocean aquatic continuum of the northeast North American coast., Biogeosciences, 12, 1447–1458, https://doi.org/10.5194/bg-12-1447-2015, 2015.

Laruelle, G. G., Landschützer, P., Gruber, N., Tison, J.-L., Delille, B., and Regnier, P.: Global high-resolution monthly pCO_2 climatology for the coastal ocean derived from neural network interpolation, Biogeosciences, 14, 4545–4561, https://doi.org/10.5194/bg-14-4545-2017, 2017 (data available at: https://doi.org/10.5194/bg-14-4545-2017-supplement).

Laruelle, G. G., Cai, W.-J., Hu, X., Gruber, N., Mackenzie, F. T., and Regnier, P.: Continental shelves as a variable but increasing global sink for atmospheric carbon dioxide, Nat. Commun., 9, 454, https://doi.org/10.1038/s41467-017-02738-z, 2018.

Lewis, E. R. and Wallace, D. W. R.: Program Developed for CO_2 System Calculations, CDIAC, ESS-DIVE repository [data set], https://doi.org/10.15485/1464255, 1998.

Liao, E., Resplandy, L., Liu, J., and Bowman, K. W.: Amplification of the Ocean Carbon Sink During El Niños: Role of Poleward Ekman Transport and Influence on Atmospheric CO_2, Global Biogeochem. Cy., 34, e2020GB006574, https://doi.org/10.1029/2020GB006574, 2020.

Liu, K. K., Atkinson, L., Quiñones, R., and Talaue-McManus, L.: Carbon and Nutrient Fluxes in Continental Margins, Global Change – The IGBP Series, Earth and Environmental Science, Springer Berlin Heidelberg, 741 pp., https://doi.org/10.1007/978-3-540-92735-8, 2010.

Locarnini, R. A., Mishonov, A. V., Antonov, J. I., Boyer, T. P., Garcia, H. E., Baranova, O. K., Zweng, M. M., Paver, C. R., Reagan, J. R., Johnson, D. R., Hamilton, M., and Seidov, D.: Temperature, World ocean atlas 2013, NOAA Atlas NESDIS 73, Volume 1, Ocean Climate Laboratory, National Oceanographic Data Center, 40 pp., https://doi.org/10.7289/V55X26VD, 2013.

Lovenduski, N. S., Gruber, N., Doney, S. C., and Lima, I. D.: Enhanced CO_2 outgassing in the Southern Ocean from a positive phase of the Southern Annular Mode, Global Biogeochem. Cy., 21, GB2026, https://doi.org/10.1029/2006GB002900, 2007.

Mackenzie, F. T., Andersson, A. J., Lerman, A., and Ver, L. M.: Boundary exchanges in the global coastal margin: implications for the organic and inorganic carbon cycles, in: The sea, vol. 13, edited by: Robinson, A. R. and Brink, K. H., Harvard University Press, Cambridge, MA, 193–225, 2005.

Manning, A. C. and Keeling, R. F.: Global oceanic and land biotic carbon sinks from the scripps atmospheric oxygen flask sampling network, Tellus B, 58, 95–116, https://doi.org/10.1111/j.1600-0889.2006.00175.x, 2006.

Masarie, K. A., Hall, F. G., Collatz, G. J., Meeson, B. W., Los, S. O., Brown De Colstoun, E., and Landis, D. R.: ISLSCP II Globalview: Atmospheric CO_2 Concentrations. ORNL DAAC, Oak Ridge, Tennessee, USA [data set], https://doi.org/10.3334/ORNLDAAC/1111, 2012.

McGregor, H. V., Dima, M., Fischer, H. W., and Mulitza, S.: Rapid 20th-century increase in coastal upwelling off northwest Africa, Science, 315, 637–639, https://doi.org/10.1126/science.1134839, 2007.

Millero, F. J.: Carbonate constants for estuarine waters, Mar. Freshwater Res., 61, 139–142, https://doi.org/10.1071/MF09254, 2010.

Nakaoka, S. I., Aoki, S., Nakazawa, T., Hashida, G., Morimoto, S., Yamanouchi, T., and Yoshikawa-Inoue, H.: Temporal and spatial variations of oceanic pCO_2 and air-sea CO_2 flux in the Greenland Sea and the Barents Sea, Tellus B, 58, 148–161, https://doi.org/10.1111/j.1600-0889.2006.00178.x, 2006.

O'Mara, N. A. and Dunne, J. P.: Hot Spots of Carbon and Alkalinity Cycling in the Coastal Oceans, Sci. Rep., 9, 4434, https://doi.org/10.1038/s41598-019-41064-w, 2019.

Olsen, A., Key, R. M., van Heuven, S., Lauvset, S. K., Velo, A., Lin, X., Schirnick, C., Kozyr, A., Tanhua, T., Hoppema, M., Jutterström, S., Steinfeldt, R., Jeansson, E., Ishii, M., Pérez, F. F., and Suzuki, T.: The Global Ocean Data Analysis Project version 2 (GLODAPv2) – an internally consistent data product for the world ocean, Earth Syst. Sci. Data, 8, 297–323, https://doi.org/10.5194/essd-8-297-2016, 2016.

Regnier, P., Friedlingstein, P., Ciais, P., Mackenzie, F. T., Gruber, N., Janssens, I. A., Laruelle, G. G., Lauerwald, R., Luyssaert, S., Andersson, A. J., Arndt, S., Arnosti, C., Borges, A. V, Dale, A. W., Gallego-Sala, A., Goddéris, Y., Goossens, N., Hartmann, J., Heinze, C., Ilyina, T., Joos, F., LaRowe, D. E., Leifeld, J., Meysman, F. J. R., Munhoven, G., Raymond, P. A., Spahni, R., Suntharalingam, P., and Thullner, M.: Anthropogenic perturbation of the carbon fluxes from land to ocean, Nat. Geosci., 6, 597–607, https://doi.org/10.1038/ngeo1830, 2013.

Reynolds, R. W., Smith, T. M., Liu, C., Chelton, D. B., Casey, K. S., and Schlax, M. G.: Daily high-resolution-blended analyses for sea surface temperature, J. Clim., 20, 5473–5496, https://doi.org/10.1175/2007JCLI1824.1, 2007 (data available at: https://psl.noaa.gov/data/gridded/data.noaa.oisst.v2.highres.html, last access: March 2021).

Rödenbeck, C., Bakker, D. C. E., Metzl, N., Olsen, A., Sabine, C., Cassar, N., Reum, F., Keeling, R. F., and Heimann, M.: Interannual sea–air CO_2 flux variability from an observation-driven ocean mixed-layer scheme, Biogeosciences, 11, 4599–4613, https://doi.org/10.5194/bg-11-4599-2014, 2014.

Rödenbeck, C., Bakker, D. C. E., Gruber, N., Iida, Y., Jacobson, A. R., Jones, S., Landschützer, P., Metzl, N., Nakaoka, S., Olsen, A., Park, G.-H., Peylin, P., Rodgers, K. B., Sasse, T. P., Schuster, U., Shutler, J. D., Valsala, V., Wanninkhof, R., and Zeng, J.: Data-based estimates of the ocean carbon sink variability – first results of the Surface Ocean pCO_2 Mapping intercomparison (SOCOM), Biogeosciences, 12, 7251–7278, https://doi.org/10.5194/bg-12-7251-2015, 2015.

Roobaert, A., Laruelle, G. G., Landschützer, P., Gruber, N., Chou, L., and Regnier, P.: The Spatiotemporal Dynamics of the Sources and Sinks of CO_2 in the Global Coastal Ocean, Global Biogeochem. Cy., 33, 1693–1714, https://doi.org/10.1029/2019GB006239, 2019.

Sarmiento, J. L. and Gruber, N.: Ocean Biogeochemical Dynamics, Princeton University Press, NJ, 526 pp., ISBN 978-0691017075, 2006.

Seitzinger, S. P., Harrison, J. A., Dumont, E., Beusen, A. H. W., and Bouwman, A. F.: Sources and delivery of carbon, nitrogen, and phosphorus to the coastal zone: An overview of Global Nutrient Export from Watersheds (NEWS) models and their application, Global Biogeochem. Cy., 19, GB4S01, https://doi.org/10.1029/2005GB002606, 2005.

Shadwick, E. H., Thomas, H., Comeau, A., Craig, S. E., Hunt, C. W., and Salisbury, J. E.: Air-Sea CO_2 fluxes on the Scotian Shelf: seasonal to multi-annual variability, Biogeosciences, 7, 3851–3867, https://doi.org/10.5194/bg-7-3851-2010, 2010.

Shadwick, E. H., Thomas, H., Azetsu-Scott, K., Greenan, B. J. W., Head, E., and Horne, E.: Seasonal variability of dissolved inorganic carbon and surface water pCO_2 in the Scotian Shelf region of the Northwestern Atlantic, Mar. Chem., 124, 23–37, https://doi.org/10.1016/j.marchem.2010.11.004, 2011.

Signorini, S. R., Mannino, A., Najjar, R. G., Friedrichs, M. A. M., Cai, W. J., Salisbury, J., Wang, Z. A., Thomas, H., and Shadwick, E.: Surface ocean pCO_2 seasonality and sea-air CO_2 flux estimates for the North American east coast, J. Geophys. Res.-Ocean., 118, 5439–5460, https://doi.org/10.1002/jgrc.20369, 2013.

Stock, C. A., Dunne, J. P., and John, J. G.: Global-scale carbon and energy flows through the marine planktonic food web: An anal-

ysis with a coupled physical-biological model, Prog. Oceanogr., 120, 1–28, https://doi.org/10.1016/j.pocean.2013.07.001, 2014.

Stock, C. A., Dunne, J. P., Fan, S., Ginoux, P., John, J., Krasting, J. P., Laufkötter, C., Paulot, F., and Zadeh, N.: Ocean Biogeochemistry in GFDL's Earth System Model 4.1 and Its Response to Increasing Atmospheric CO_2, J. Adv. Model. Earth Sy., 12, e2019MS002043, https://doi.org/10.1029/2019MS002043, 2020.

Takahashi, T., Olafsson, J., Goddard, J. G., Chipman, D. W., and Sutherland, S. C.: Seasonal variation of CO_2 and nutrients in the high-latitude surface oceans: A comparative study, Global Biogeochem. Cy., 7, 843–878, https://doi.org/10.1029/93GB02263, 1993.

Takahashi, T., Sutherland, S. C., Sweeney, C., Poisson, A., Metzl, N., Tilbrook, B., Bates, N., Wanninkhof, R., Feely, R., Sabine, C., Olafsson, J., and Nojiri, Y.: Global sea – air CO_2 flux based on climatological surface ocean pCO_2, and seasonal biological and temperature effects, Deep Sea Res. Pt. II, 49, 1601–1622, https://doi.org/10.1016/S0967-0645(02)00003-6, 2002.

Takahashi, T., Sutherland, S. C., and Kozyr, A.: Global Ocean Surface Water Partial Pressure of CO_2 Database: Measurements Performed During 1957–2011 (Version 2011), ORNL/CDIAC-160, NDP-088(V2011), Carbon Dioxide Information Analysis Center, Oak Ridge National Laboratory, U.S. Department of Energy, Oak Ridge, Tennessee [data set], available at: https://cdiac.ess-dive.lbl.gov/ftp/oceans/LDEO_Database/Version_2011/ (last access: March 2021), 2012.

Tsujino, H., Urakawa, S., Nakano, H., Small, R. J., Kim, W. M., Yeager, S. G., Danabasoglu, G., Suzuki, T., Bamber, J. L., Bentsen, M., Böning, C. W., Bozec, A., Chassignet, E. P., Curchitser, E., Boeira Dias, F., Durack, P. J., Griffies, S. M., Harada, Y., Ilicak, M., Josey, S. A., Kobayashi, C., Kobayashi, S., Komuro, Y., Large, W. G., Le Sommer, J., Marsland, S. J., Masina, S., Scheinert, M., Tomita, H., Valdivieso, M., and Yamazaki, D.: JRA-55 based surface dataset for driving ocean–sea-ice models (JRA55-do), Ocean Model., 130, 79–139, https://doi.org/10.1016/j.ocemod.2018.07.002, 2018.

Turi, G., Lachkar, Z., and Gruber, N.: Spatiotemporal variability and drivers of pCO_2 and air–sea CO_2 fluxes in the California Current System: an eddy-resolving modeling study, Biogeosciences, 11, 671–690, https://doi.org/10.5194/bg-11-671-2014, 2014.

Wolf-Gladrow, D. A., Zeebe, R. E., Klaas, C., Körtzinger, A., and Dickson, A. G.: Total alkalinity: The explicit conservative expression and its application to biogeochemical processes, Mar. Chem., 106, 287–300, https://doi.org/10.1016/j.marchem.2007.01.006, 2007.

Yasunaka, S., Murata, A., Watanabe, E., Chierici, M., Fransson, A., van Heuven, S., Hoppema, M., Ishii, M., Johannessen, T., Kosugi, N., Lauvset, S. K., Mathis, J. T., Nishino, S., Omar, A. M., Olsen, A., Sasano, D., Takahashi, T., and Wanninkhof, R.: Mapping of the air-sea CO_2 flux in the Arctic Ocean and its adjacent seas: Basin-wide distribution and seasonal to interannual variability, Polar Sci., 10, 323–334, https://doi.org/10.1016/j.polar.2016.03.006, 2016.

Zweng, M. M., Reagan, J. R., Antonov, J. I., Locarnini, R. A., Mishonov, A. V., Boyer, T. P., Garcia, H. E., Baranova, O. K., Johnson, D. R., Seidov, D., and Biddle, M. M.: World ocean atlas 2013, NOAA Atlas NESDIS 74, Volume 2: Salinity, edited by: Levitus, S. and Mishonov, A. (technical editor), Ocean Climate Laboratory, National Oceanographic Data Center, 39 pp., https://doi.org/10.7289/V5251G4D, 2013.